



University of Crete
and
Hellenic Mediterranean University

Master Thesis

Laser Induced Graphene on Polyimide substrate for hydrogen generation

---

Candidate Name:
Theodora Gounela

Supervisor:
Dr. Maria Pervolaraki

A thesis submitted for the fulfillment of the requirements
for the degree of Masters in Nanotechnology for Energy Applications
in the

Laser Materials Synthesis and Space Research Group (LMSS)

Foundation of Research and Technology (FORTH)

February, 2025

Abstract

Graphene, a remarkably versatile material with diverse properties and applications, has been synthesized through various chemical methods. In 2004, studies on ablation techniques, particularly the work by Dyer, Pervolaraki, and Lippert, introduced the fabrication of protruding carbon structures on polyimide substrates using laser sources. Their research investigated the thermal modeling and experimental outcomes of laser interactions with polyimide, highlighting processes that lead to polymer carbonization, a key aspect of Laser-Induced Graphene (LIG) production. Although this study contributed to the understanding of carbon-rich material formation, it was not until 2014 that James Tour and his team at Rice University published the first formal report identifying the resulting material as LIG due to its graphene-like properties. This marked a significant advancement, prompting extensive investigations into optimizing the production of LIG for enhanced quality. This LIG synthesis method represents a one-step, environmentally sustainable technique that requires a high-powered laser and an organic polymeric substrate, such as polyimide (PI). This method offers a promising green alternative to the complex and resource-intensive processes previously employed. However, achieving high-quality graphene while minimizing resistivity remains a challenge, as LIG synthesis is inherently sensitive and relies on precise control of parameters such as laser wavelength, fluence, spot size, and duration of substrate irradiation.

This thesis work focuses on the optimization of LIG fabrication parameters for the production of low-resistivity electrodes for electrochemical hydrogen generation. Utilizing commercially available PI as a substrate and nanosecond and picosecond pulses from a commercial laser, high-quality LIG was fabricated after an optimization process that tested different repetition rates, powers, pulse durations, and laser pattern parameters. The lowest sheet resistance reached values of 16 Ω/sq, and its superior quality was confirmed by I-V and Raman measurements as well as SEM images. To test pure and functionalized LIG, several samples were used as electrodes for the Hydrogen Evolution Reaction (HER), and performance was quantified through Linear Sweep Voltammetry (LSV) and Chronoamperometry (CA). It was observed that pure LIG films performed better than porphyrin-functionalized LIG samples, which was attributed to the less exposed porous surface of the electrode, resulting in poor contact between the conductive film and the electrolyte. Further optimization could improve the performance of LIG in hydrogen generation as well as in other applications such as water filtration.

I would like to dedicate this thesis to my dearest family, your unwavering support and belief in me have been my guiding light throughout this journey.
To my cherished friends and colleagues, thank you for the laughter and shared memories that eased the challenges.
And last but not least, my partner, your patience, encouragement, and sage advice have lifted me up when I faltered and inspired me to reach for greater heights. Thank you for being my anchor through it all.

This thesis is dedicated to each of you, with heartfelt gratitude for your unwavering support and love.

Acknowledgments

This thesis would not have been possible without the guidance and the help of several individuals who in one way or another contributed and extended their valuable assistance in the preparation and completion of this study, it is a pleasure to thank those who made it possible.

I would like to express my sincere gratitude to Dr. Maria Pervolaraki for her invaluable guidance, support, and encouragement throughout the entire process of completing this master thesis. Her expertise, insights, and unwavering commitment have been instrumental in shaping this work. Appreciation is also due to Dr. Emmanouil Stratakis, deputy director of FORTH-IESL, for providing the necessary laboratory equipment and consistently offering assistance whenever needed

Special thanks are given to Dr. G. Kenanakis and Ms. Clyto Katsara for their essential contributions in conducting the Raman measurements for this study. Additionally, thanks to Ms. Aleka Manousaki for providing the SEM images that greatly aided in the characterization of the materials. Their support has been invaluable to the success of this research.

Gratitude is expressed to the senior researchers, peers, and collaborators who have been very helpful during my master's study.

Special thanks are extended to George Karathanasopoulos, master student in the LMSS subgroup and colleague, for his assistance and sharing of his engineering and IT knowledge and advice.

Lastly I would like to thank Manos Nickoloudakis for his contributions to the hydrogen generation applications of the resulting LIG material.

Contents

Abbreviations 7

1. Introduction 9

2. Theory and Materials

2.1 Graphene

2.1.1 Electrical Properties 9
2.1.2 Optical Properties 10
2.1.3 Fabrication 11

2.2 Laser-Induced Graphene

2.2.1 LIG Fabrication Principles 12
2.2.2 PI as a Substrate for LIG Fabrication 14
2.2.3 Applications 16

2.3 Laser Gaussian Beams 18

3. Experimental Methods

3.1 Laser Source 20

3.2 Characterization Techniques

3.2.1 Electrical measurements 21
3.2.2 Scanning Electron Microscopy 22
3.2.3 Raman Spectroscopy 22

3.3 Optical Setups

3.3.1 First Setup (3D Printer stage) 23
3.3.2 Second Setup (Dedicated XY stage) 24

3.4 LIG in Hydrogen Generation

3.4.1 Hydrogen Evolution Reaction 24
3.4.2 Porphyrin Functionalization (HER) 25
3.4.3 HER efficiency measurement methods 26

4. Results & Discussion

4.1 Laser characterization 27

4.1.1 Humidity and Lasers 28

4.2 LIG Optimization & Characterization

4.2.1 First Setup (3D Printer Stage) 29
4.2.2 Second Setup (Dedicated XY Stage) 32

4.3 Comparison of State-of-the-Art LIG from different laser types 37

4.4 LIG as Electrodes in Hydrogen Generation 39

5. Conclusions 42

6. Future Prospects 44

7. References 48

Abbreviations

LIG	Laser Induced Graphene
PI	Polyimide
HR-SEM	High Resolution Scanning Electron Microscopy
HER	Hydrogen Evolution Reaction
OER	Oxygen Evolution Reaction
BZ	Brillouin Zone
CoTPP	Cobalt(II) tetraphenylporphyrin
CuTPP	Copper(II) tetraphenylporphyrin
THF	Tetrahydrofuran
TPP	Tetraphenylporphyrin
LSV	Linear sweep voltammetry technique
CA	Chronoamperometry technique

CHAPTER 1

Introduction

Since its discovery in 2004, graphene, a two dimensional (2D) carbon allotrope has sparked significant interest in both the scientific and industrial realms. Its distinct features, resulting from a single layer of carbon atoms organized in a hexagonal lattice, have established it as a revolutionary material with enormous potential in a wide range of sectors.

In 1959, Richard Feynman delivered an influential lecture titled "There's Plenty of Room at the Bottom." In this speech, Feynman imagined a groundbreaking advance in physics. His inquiries posed challenges to scientists, including physicists Andre K. Geim and Konstantin S. Novoselov, who, 45 years later in 2004, at the University of Manchester, successfully isolated graphene, a single atomic layer of carbon, using Scotch tape method [1], [2].

Graphitization of polymers by laser ablation was explored by Dyer, Pervolaraki, and Lippert, in a study that showed protruding carbon structures on polyimide after controlled ablation [3]. In 2014, Prof. James Tour and his team [4] coined the termed LIG to describe the highly conductive porous 3D multilayer graphene foam resulting from controlled laser-induced burning. This method utilized a commercial laser scribing system commonly available in machine shops to directly convert PI plastic films into 3D porous graphene, refred to as LIG, by employing a CO_2 infrared laser to directly scan a commercial PI film, as depicted in ***Figure 1.1***. This laser treatment induces vibrational excitation within the internal structure of the irradiated PI, resulting in localized temperature increases that break C–O, C–, and N–C bonds. Consequently, carbon atoms undergo reorganization, to form the graphene structure. Simultaneously, the remaining carbon, oxygen, and nitrogen atoms recombine and are emitted as gaseous byproducts including CO, CO_2, and NO. Notably, while carbon atoms tend to form rings during this process, maintaining stability within such a brief reaction period presents challenges. This instability leads to the formation of rings that deviate from the typical hexagonal structure of graphene, resulting in a mixture of polygons, that includes locally flawed five- and seven-membered carbon rings alongside the standard six-membered carbon rings of graphene [5], [6].

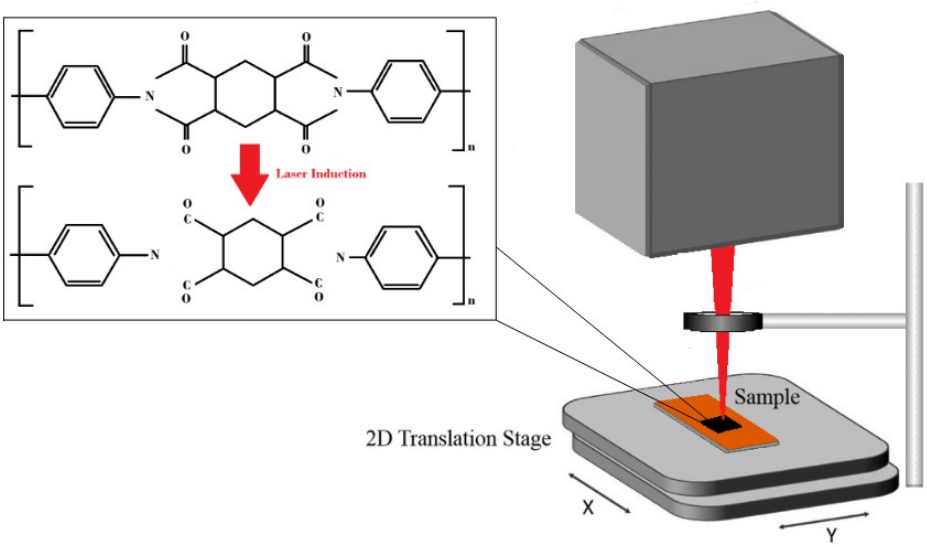


Figure 1.1. *Schematic of LIG fabricated on PI films.*

LIG is not restricted to a limited number of layers of the sp^2 carbon lattice. While pristine graphene exhibits remarkable properties, three-dimensional porous graphene (LIG) is often favored for various applications due to its straightforward synthesis and cost-effectiveness. Furthermore, the presence of structural defects within graphene sheets facilitates material doping and functionalization. For instance, the oxygen content on the surface of LIG can be adjusted to modify its surface wettability [7].

LIG is flexible just like pure graphene, but is characterized by a highly porous structure, making it ideal for applications in water ultrafiltration. LIG's porosity makes it able to permeate water and other liquid solvents, separating particles or bacteria larger than the pores of the material. Water ultrafiltration membranes based on LIG have been demonstrated, which showed high water permeability and rejection. LIG membranes fabricated from poly(ether sulfone) (PES) membranes, treated with glycerol were tested for water permeability and rejection of bovine serum albumin, a protein often used in lab experiments, and results showed high permeability for LIG membranes and rejection reaching 92.8% [8], higher than other filtration membranes, like ones based on Graphene Oxide (GO) [9]. In another study, LIG fabricated from PI coupled with TiO_2 microfiltration ceramic discs, showed higher permeability for non-polar solvents (hexane) than polar solvents (water), with rejection of particles larger than 250 μm, at 90% [10], highlighting the capability of LIG membranes for not only water, but also lab solvent permeation. The high electrical conductivity and high surface area resulting from the porous structure of LIG make it suitable for use as electrodes in many applications, including supercapacitors [11], and hydrogen generation through electrolysis. These properties of LIG facilitate enhanced contact and charge transfer between electrolytes. LIG fabricated from Pt doped PI, has demonstrated effective water splitting [12]. Recent studies indicate that while LIG is highly efficient for hydrogen evolution reaction (HER), the oxygen evolution reaction (OER) can lead to degradation of the bare LIG electrode [13]. Graphitization of the surrounding PI substrate by heating under vacuum to convert the substrate from insulating to conducting, was later shown to further increase the efficiency of LIG electrodes in hydrogen generation [14].

CHAPTER 2

Theory & Materials

2.1 Graphene

Graphene's exceptional mechanical, electrical, thermal, and optical properties distinguish it as a material of unparalleled versatility. It comprises a sp^2 hybridized hexagonal honeycomb carbon structure with a carbon-carbon distance of 1.42 Å [15]. The extraordinary electronic properties of graphene, combined with its structural flexibility, manifest in its outstanding conductivity, strength, and adaptability. Graphene's extraordinary electrical conductivity, coupled with high electron mobility at room temperature, has positioned it at the forefront of nanoelectronics and optoelectronics, offering the potential for faster, more efficient devices with reduced energy consumption. Its exceptional thermal conductivity (5000 W m^{-1} K^{-1}) and outstanding mechanical properties, including a Young's modulus of 1 TPa, make it an ideal material for heat dissipation in electronics and thermal management across various applications. Additionally, graphene's transparency and impermeability make it suitable for applications in transparent conductive films, anti-corrosion coatings, and barrier materials. Moreover, by reducing the dimensions of graphene into narrow ribbons with a width of 1–2 nm, a distinct band gap can be generated, yielding semi-conductive graphene with potential applications in transistors [16], [17].

2.1.1 Electronic properties

2D graphene's band structure was first explored by R. P. Wallace [18], showing its unusual semimetallic behavior. Graphene is made out of carbon atoms arranged in hexagonal structure, with real space basis vectors a_1, a_2 depending on a, the nearest neighbor distance (1.42 Å):

2.1 $$a_1=\frac{a}{2}(3,\sqrt{3}),a_2=\frac{a}{2}(3,-\sqrt{3})$$

that give rise to a triangular unit cell, containing two carbon atoms (***Figure 2.1a***). These basis vectors can be translated to reciprocal space as the basis vectors b_1, b_2:

2.2 $$b_1=\frac{2\pi}{3a}(1,\sqrt{3}),b_2=\frac{2\pi}{3a}(1,-\sqrt{3})$$

which form the characteristic hexagonal Brillouin Zone (BZ) (***Figure 2.1b***) in momentum space. The edges of the hexagonal BZ are named K-, K'-points, crucial for graphene's transport characteristics. The positions of these points are:

2.3 $$K=\left(\frac{2\pi}{3a},\frac{2\pi}{3\sqrt{3}a}\right),K'=\left(\frac{2\pi}{3a},-\frac{2\pi}{3\sqrt{3}a}\right)$$

Carriers in the graphene lattice can hop from carbon atom to nearest or second nearest neighboring atom, with γ_0 (2.8 eV) and γ_0' the nearest and next-nearest neighbor hopping energies respectively. The energy dispersion relations are derived from the tight-binding model as:

2.4
$$E_{\pm}(k) = \pm\gamma_0\sqrt{3+f(k)} - \gamma_0' f(k)$$

$$\text{with } f(k) = 2\cos\left(\sqrt{3}k_y a\right) + 4\cos\left(\frac{\sqrt{3}}{2}k_y a\right)\cos\left(\frac{3}{2}k_x a\right)$$

where the plus and minus signs refer to the upper (π*) and lower (π) bands, and k is the momentum. The energy dispersion of graphene is shown in **Figure 2.1c**, where it is obvious that the conduction and valence bands touch at the K-points of the momentum space, at 0, which are called Dirac points.

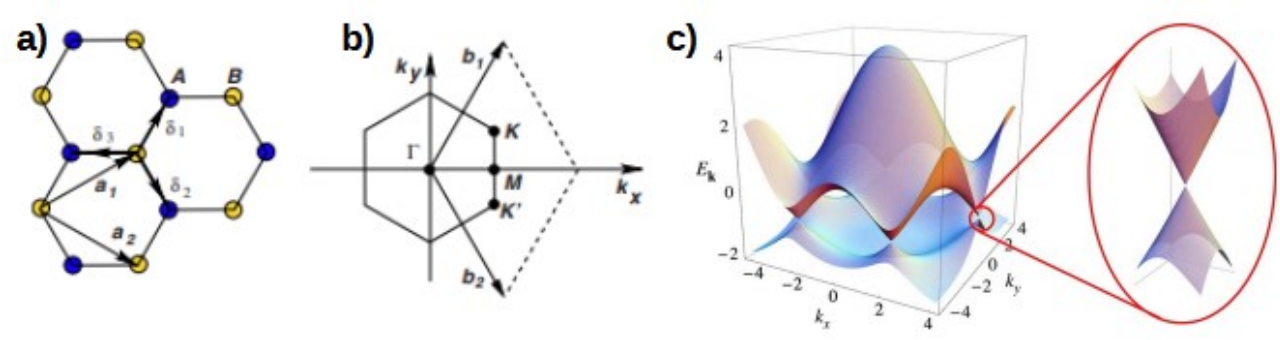


Figure 2.1. (a) Graphene lattice with basis vectors a_1, a_2 **(b)** Hexagonal Brillouin Zone of graphene, resulting from the reciprocal vectors b_1, b_2 **(c)** Electronic dispersion in the graphene lattice, emphasizing the Dirac Points. [15]

Due to its unique band structure, electrons in graphene can move through the lattice with Fermi velocity $v_F = 10^6$ m/s [15], in the ballistic transport regime, resulting in mobilities up to 200000 $cm^2 V^{-1} s^{-1}$ [19]. This makes graphene an atomic layer conductor with extremely high mobilities.

2.1.2 Optical Properties

Graphene's optical transitions, integral to its distinctive characteristics, stem from the material's unique band structure. The linear dispersion relation near the Dirac points defines the band structure, resulting in a zero band gap, as already mentioned. The optical transitions between the valence and the conduction bands are known as interband transitions and because of the zero band gap of pristine graphene, these transitions can occur across the visible spectral range. The intraband transitions involve processes where electrons within either the conduction or valence band absorb or emit photons, leading to changes in their energy levels, prominent at higher photon energies or in the far-infrared region [20]. Due to interband and intraband transitions graphene can absorb light across a broad spectrum, ranging from ultraviolet and visible to infrared and terahertz regions. Specifically graphene absorbs around 2.3% of incident light in the visible to near-infrared region because of the interband transitions.

Plasmons are collective oscillations of free electrons in a material in response to an external electromagnetic field exert a profound influence on the optical properties of graphene. Remarkably, graphene retains exceptional transparency in the visible range due to the specific energy distribution of its plasmonic response. However, in the middle infrared region, graphene becomes more

transparent to light because interband transitions are suppressed. In the far infrared region, graphene can reflect and absorb light due to the coupling between free carriers and electromagnetic waves. Additionally, in the lower frequency region such as the infrared and THz region, graphene exhibits a negative permittivity with ohmic losses. The negative permittivity, which is the negative value of a measure of a material's ability to allow the electric field to penetrate it, is associated with its unique electronic structure and the behavior of its charge carriers and is closely tied to the excitation of plasmons. Plasmons in graphene, as collective oscillations of free electrons, can lead to negative permittivity within specific frequency regions. However, the resistive nature of graphene results in the conversion of a portion of the absorbed energy into heat, resulting in ohmic losses. This interplay between negative permittivity and ohmic losses is a critical aspect of graphene's optical response and plasmonic behavior. By manipulating the Fermi level through doping or electrostatic gating, the plasmonic characteristics of graphene can be tuned, allowing control over the material's reflectivity. Understanding and harnessing these plasmonic effects not only enhances the comprehension of graphene's optical behavior, but also paves the way for tailored applications in transparent conductive films, terahertz devices, and optoelectronics. [19]

The atomic scale of graphene, while advantageous for many applications, imposes constraints in terms of light absorption and interaction. The absence of an electronic band gap—a distinctive feature of graphene— limits its ability to absorb light in a manner comparable to traditional semiconductors. Additionally, the single-atom thickness may restrict the overall cross-sectional area available for light interaction, thereby influencing the material's efficiency in certain optical processes [21]. To enhance the interaction, photoactive substrates such as quantum dots, optical cavities, waveguides, plasmonic nanostructures, and photonic crystals can be employed [19]. The multifaceted properties of graphene underscore its significance in advancing material science and technology, paving the way for innovations in electronics, optoelectronics, and other fields [19].

2.1.3 Fabrication Methods

Aside from its instinct properties graphene is popular because of its ease fabrication techniques such as mechanical exfoliation, chemical vapor deposition, and epitaxial growth enable the production of graphene with tailored characteristics, suitable for specific applications. Moreover, the ability to modify graphene's surface chemistry through doping, functionalization, and nanostructuring enhances its compatibility with diverse matrices and facilitates integration into existing technologies.

Various techniques have been developed for the fabrication of graphene, each with its own advantages and short-comings. Epitaxial growth on silicon carbide (SiC) and metal substrates like ruthenium and platinum at high temperatures and ultra-high vacuum conditions enables the production of large-sized, high-quality graphene. However, this method poses challenges in achieving high yields and transferring graphene to substrates, due to the high vacuum and costly manufacturing systems involved [5]. Chemical vapor deposition (CVD) is another method that allows for the growth of highly crystalline, nearly defect-free graphene [22]. Similar to epitaxial growth, CVD requires high temperatures, which limits the choice of suitable substrates and often necessitates additional transfer processes for temperature-sensitive substrates like plastics. Chemical stripping, involving the oxidation, intercalation, exfoliation, and reduction of graphene derivatives, offers an attractive approach for large-scale graphene production. Despite its low cost, this method

typically results in graphene that lacks a patterned structure, requiring further reduction processes to achieve high purity. The challenge persists in terms on balancing graphene quality with fabrication using these conventional methods [23], [24].

Recently, laser processing technology has emerged as a powerful tool in various fields, ranging from industry to medical science. In direct laser writing (DLW) a focused laser beam can precisely induce photothermal and photochemical reactions in a very small area, achieving results that are difficult to obtain with conventional thermal treatments that depend on the laser processing parameters and material properties. DLW is distinguished as a fabrication technique that eliminates the need for lithography, masks, or toxic etching chemicals. This approach enhances design flexibility, productivity, and environmental sustainability, while also reducing raw material consumption and minimizing environmental impact. Compared to traditional synthesis and patterning techniques, DLW offers numerous advantages including high spatial resolution, non-contact processing, scalability, high productivity, low energy consumption, cost-effectiveness, and compatibility with three-dimensional structures. These attributes make DLW a superior method for graphene fabrication [7].

2.2 Laser-Induced Graphene (LIG)

LIG is a form of graphene structure synthesized through laser irradiation. This method involves heating the material with lasers, thereby inducing a transformation into a three-dimensional carbon structure. Given this technique is a one-step process, LIG synthesis has garnered significant interest owing to its properties, which closely resemble those of pure graphene. It is commonly produced on thermoplastic polymers like polyimide (PI), polyetherimide (PEI) [4], poly(ether- ether- ketone) (PEEK) [25], and polyether sulfone (PES) [26] and presents an appealing flexibility, low cost and ease of manufacture, reasons for which it is considered a suitable candidate for flexible electronics applications [11], [27].

2.2.1 LIG Fabrication principles

Unlike traditional approaches, this one-step process does not require high-temperature reaction conditions, solvents, or subsequent treatments, resulting in graphene that contains numerous five- and seven-membered rings [25]. Referred to as "kinetic graphene", LIG maintains its atomic arrangement without the need for annealing, offering versatility in morphology control, including the production of porous sheets or fibrils, as well as the manipulation of porosity, composition, and surface properties [28], [29]. This fabrication method integrates both the creation and shaping of graphene in one step, eliminating the necessity for costly cleanroom equipment, chemical procedures, or labor-intensive post-processing. Furthermore, the shape of LIG designs can be easily adjusted using software, making it well-suited for adaptable and scalable manufacturing [7].

The laser treatment induces vibrational excitation within the internal lattice of the irradiated polyimide, leading to localized temperatures that, in some cases, exceed 2500°C. This elevated temperature causes the rupture of C–O, C=O, and N–C bonds within the material. Concurrently, the remaining carbon, oxygen, and nitrogen atoms recombine and are released as gases such as carbon monoxide (CO), carbon dioxide (CO_2), and nitrogen monoxide (NO) [6]. Notably, despite the rearrangement of carbon atoms into rings, maintaining stability within such a brief reaction time proves challenging, resulting in rings that do not exhibit the typical hexagonal structure of

graphene. Instead, a mixed polygonal structure emerges, comprising locally defective five- and seven-membered carbon rings alongside the six-membered carbon rings characteristic of typical graphene [5], [6]. This specific structure, and characteristics of LIG are influenced by variables like fabrication conditions and the precursor materials [6]. The chemical reactions and resulting changes depend on the nature and composition of the substrates, enabling the creation of LIG with tailored properties [30]. The structure of LIG is characterized by pores, formed from rapid gas production under laser exposure. LIG is not limited to a single or few layers of sp^2 carbon lattice. While perfect single-layer graphene has excellent properties, 3D porous graphene (LIG) is preferred for many applications due to its simple preparation and low production costs. Additionally, structural defects in graphene sheets enable material doping and functionalization , like tuning oxygen content on the surface of LIG to modify surface wettability, essential for various applications [6].

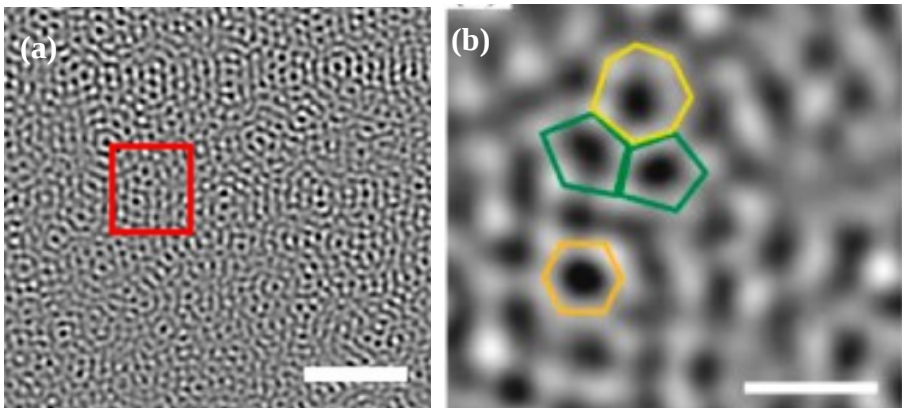


***Figure 2.2**: **(a)** TEM image of LIG showing the polygon structure. **(b)** Enlarged TEM image of the red square in (a), showing 5-, 6-, 7- membered rings [28]*

Through laser writing, it is feasible to induce the graphenization of a thin layer on the surfaces of certain materials, such as wood, by using a defocused laser spot, to avoid damage due to increased fluence. This process results in a porous structure that can be utilized as an electrode. Inspired by the formation of LIG on wood, various lignocellulosic materials—abundant and highly renewable energy resources derived from forest and agricultural biomass—have also been successfully converted into LIG under ambient conditions. This conversion facilitates the subsequent fabrication of biodegradable nanodevices [31].

Historically, lignin-containing carbon precursors have been reported to convert into LIG via laser interaction under controlled atmospheres, such as an inert or reducing gas environment. Typically, oven-dried wood comprises approximately 18−30% lignin [32]. Other natural materials, such as cork, coconut shells, and potato skins, possess even higher lignin content compared to wood, approximately 25%, 30%, and 36% lignin, respectively [31]. Multiple laser interaction processes can produce LIG on naturally occurring substrates, including cloth, paper, potato skins [33], coconut shells [34], and cork [35]. These materials are not only inexpensive and abundant but also biodegradable, making them advantageous over many polymer precursors previously identified for LIG production.

These attributes make them promising candidates for sustainable applications. Thermoplastic substrates, particularly PI and polyetherimide (PEI), have also been extensively used for the formation of LIG due to their excellent thermal stability, flexibility, and compatibility with laser processing techniques, making them highly suitable for advanced electronic applications. The

common factor between all substrates, polymers and organic materials as well, is the presence of carbon, that enables the graphitization process.

Polyimide (PI) was first used for the formation of LIG in 2014 by Lin et al. This innovative method leveraged a CO_2 laser to convert PI into a 3D porous graphene structure in a single step. This process harnesses the material's thermal stability and the laser's ability to induce localized heating, breaking and rearranging chemical bonds to form graphene. The resulting LIG's unique properties have since attracted significant interest for applications in sensors, supercapacitors, and other advanced electronic devices [36].

2.2.2 PI as a Substrate for LIG fabrication

Polyimide (PI) is a polymer that contains aromatic sp^2 hybridized carbon, which enables ring formation of atoms and characterizes graphene. Laser treatment of this material induces local heating, and at adequately high temperatures, the chemical bonds in the polymer break or rearrange, releasing gaseous byproducts. During the graphitization process, surface carbon atoms are transformed from sp^3 to sp^2 dominant configurations [30].

PI are high-performance polymers of imide monomers characterized by the presence of two acyl groups (C=O) bonded to nitrogen (N). Different polycondensation reactions yield polyimides with distinct general, electrical, and mechanical properties. Due to their planar aromatic and heteroaromatic structures, polyimides are typically synthesized via the solvent method, which addresses issues of insolubility and infusibility [37].

The synthesis of aromatic polyimides was initially reported in 1908. However, significant advancements in polyimide synthesis and processing were not achieved at that time due to challenges associated with their fabrication via melt polymerization. It was not until the early 1960s that DuPont became the first company to commercially produce polyimides, utilizing pyromellitic dianhydride and 4,4’-diaminodiphenyl ether as the primary components.

The fabrication of polyimides presents significant challenges due to their low solubility in conventional solvents and elevated softening temperatures. Typically, polyimides are synthesized through a condensation reaction between a dianhydride and a diamine, conducted in a two-step process. In the initial phase, (***Step 1 Figure 2.3***) polycondensation occurs in a polar solvent at a low temperature, resulting in the formation of polyamic acid, a soluble intermediate. In the subsequent phase, (***Step 2 Figure 2.3***) the polyamic acid is converted into polyimides through the application of heat or dehydrating agents, which is critical for producing various forms, such as fibers and films [37]. Recent advancements have significantly improved the thermal stability of polyimides, attributed to the incorporation of aromatic rings in the polymer backbone or side chains. These modifications have endowed polyimides with an exceptional combination of thermal stability, mechanical toughness, and chemical resistance. The rigid chemical structure, consisting of imide and aromatic rings, provides excellent mechanical toughness, dielectric properties, and high chemical resistance [37], [38].

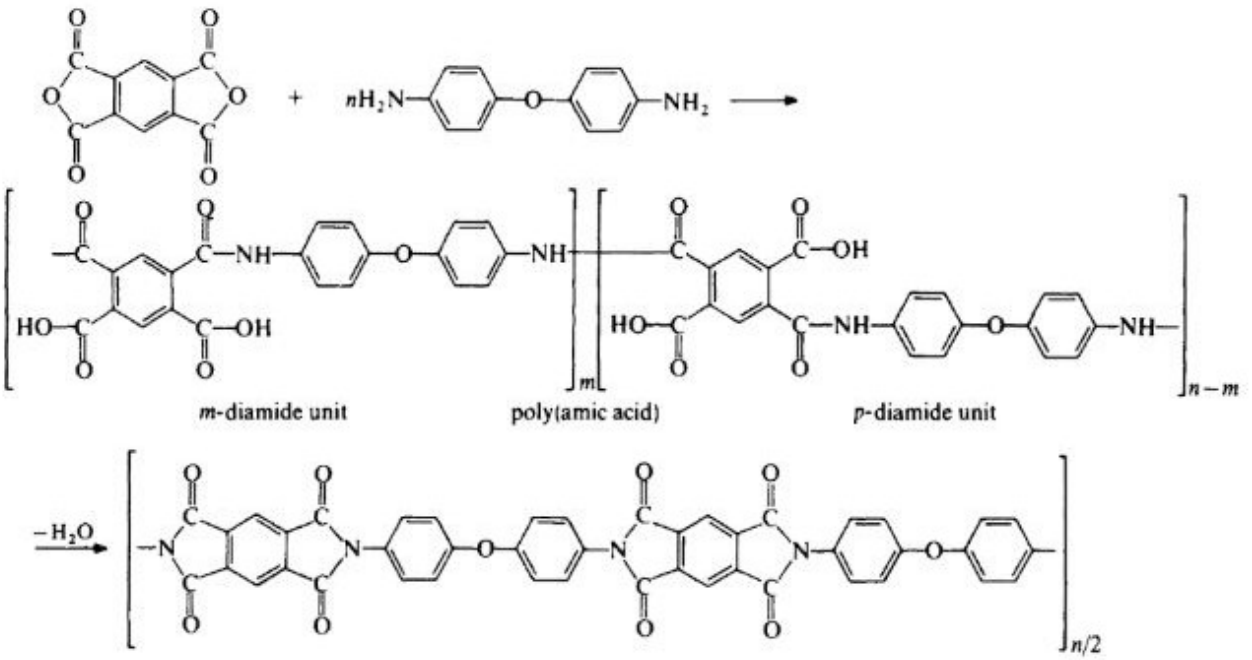


Figure 2.3. The classical method of polyimide synthesis by reaction of a dianhydride and a diamine. ***STEP 1***: Solution polycondensation of an aromatic diamine and a dianhydride to form poly(amic acid). ***STEP 2***: Poly(amic acid) could be processed into a useful shape. This is followed by cyclodehydration of the amide acid to form polyimide [37].

Polyimide films exhibit remarkable electrical properties, characterized by a high dielectric strength of 33 kV/mm, a low dielectric constant ranging from 3.2 to 4.4 and good insulation resistance,with electrical resistivity spanning from 8×10^{12} to 2×10^{15} Ω·m and sheet resistivity ranging from 100 to 10000 Ω/sq. These attributes make them ideal for use in electronics and electrical applications[37].

In terms of thermal properties, polyimides can withstand continuous use at temperatures up to 300°C while maintaining their mechanical and electrical properties over a wide temperature range. Their thermal characteristics include a coefficient of thermal expansion ranging from 9×10^{-6} to 6×10^{-5} K^{-1}, a heat deflection temperature spanning from 201 to 413.6°C, a specific heat capacity ranging from 960 to 1300 J/(kg·K), thermal conductivity between 0.31 and 0.52 W/(m·K), and a maximum service temperature of up to 260°C [38], [39]. The mechanical properties of polyimides include an elastic modulus ranging from 2.9 to 20.15 GPa, a flexural modulus between 1.1 and 510.53 GPa, flexural strength between 23.93 and 275 MPa, maximum allowed stress spanning from 85 to 250 MPa, and tensile strength ranging from 15.95 to 205 MPa.

For instance, DuPont's Kapton film, introduced in the 1960s, maintains its electrical, thermal, chemical, and mechanical properties at extreme temperatures, allowing it to be effectively used in both high and low-temperature environments where other organic polymeric materials would fail. Kapton films can also be laminated on both sides with pressure-sensitive adhesives, including acrylic and silicone [39].

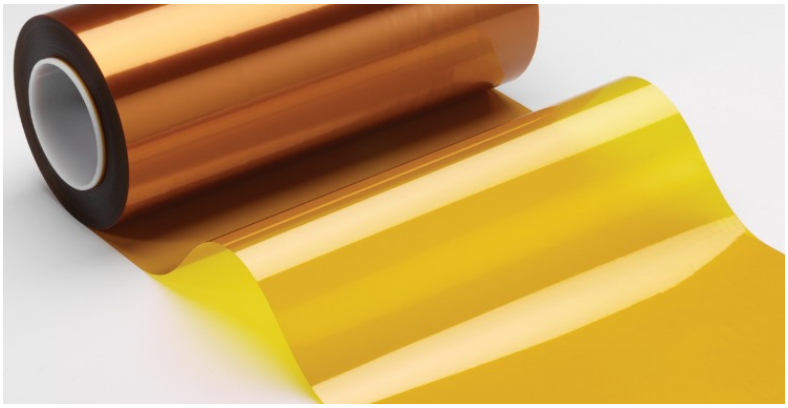


***Figure 2.4**: Polyimide Kapton Film [40]*

Aromatic heterocyclic polyimides, exemplified by commercially available polymers like DuPont's Kapton resin, are characterized by their exceptional mechanical and thermal properties, which enable them to replace certain metals and glass in high-performance applications across various industries, including electronics, automotive, and aerospace. The remarkable performance of these polyimides can be attributed to strong intermolecular forces between the polymer chains, arising from a combination of polar interactions, aromatic stacking, and charge transfer complexation. A polymer exhibiting a charge transfer complex comprises two distinct segments: a donor and an acceptor. The donor segment possesses an abundance of electrons due to nitrogen functional groups, while the acceptor segment, characterized by carbonyl groups, depletes electron density from the donor. This dynamic interaction enhances the stability of the complex and facilitates significant interactions not only between adjacent units within a single polymer chain but also across different chains. This phenomenon results in a stacking behavior akin to that of strips of paper, where donor and acceptor units are paired, effectively pulling the chains closer together. Such tight coupling enhances the structural integrity of the material [39], [41].

PI, PEEK, PEI, PES are polymers with an important similarity for LIG production, they all contain aromatic sp^2 carbon rings. However, they are different in structure and contain different atoms (oxygen, nitrogen, sulfur), making the resulting LIG different in each case. PI and PEEK are very similar polymers in terms of properties, with PI taking the lead in thermal stability, crucial for proper fabrication under high-power laser irradiation. Moreover, PI contains more gas (O, N) (**Figure 2.3**) atoms than PEEK (O), which in turn form the gaseous byproducts, and dictate the porosity of LIG. High porosity is desirable in applications such as Hydrogen generation, as it increases the available surface for interaction. Lin et. al. having tested 15 different polymers, concluded that PI is optimal for LIG fabrication, as factors like the polymerization process of each precursor affects the damage they suffer under high-powered laser beams [4].

2.2.3 LIG Applications

LIG’s unique and tailorable properties make it ideal for a wide range of applications in various fields. A prominent application of LIG is in energy storage devices, where it serves as an excellent electrode material for supercapacitors and batteries due to its high surface area and electrical conductivity. These devices achieve higher energy density through highly reversible chemical adsorption and redox reactions of electroactive substances on or within the LIG electrodes [30].

LIG derived from polyimide (PI) substrates exhibits remarkable versatility in various applications due to its unique properties. One significant application is in the field of flexible electronics, where LIG can be integrated into wearable devices that require lightweight and conformable materials. The high electrical conductivity and mechanical flexibility of LIG make it an ideal candidate for flexible circuit boards and sensors that can withstand bending and stretching without compromising performance [42]. Peng *et al.* reported a laser-generated porous graphene supercapacitor from commercial polyimide that demonstrated a stable capacitance performance at different bending curvatures and after 7000 bending cycles, exhibiting the excellent mechanical flexibility of the LIG-based electronic devices. The mechanical flexibility of LIG can be attributed to its porous structure, which consists of interconnected graphene sheets. This porous network allows LIG to deform without structural damage, as the voids can accommodate the rearrangement of graphene sheets under stress [11].

In sensor technology, LIG is used to develop flexible and efficient platforms for detecting various substances, ranging from gases to biomolecules. The detection of gases is based on thermal conductivity, measured by temperature changes caused by electrical current. The tunable electronic properties of LIG make it a promising material for electronic devices, including transistors and flexible electronics. Additionally, its lightweight and robust nature make LIG suitable for aerospace applications, such as lightweight components and sensors. The porous structure of LIG also enhances its performance in various applications by providing increased surface area for interaction with target analytes and improving charge transport properties [43], [44]. Its high surface area facilitates enhanced interaction with analytes, leading to improved sensitivity and detection limits. For instance, LIG-based sensors have been developed for the detection of glucose and other biomolecules, demonstrating rapid response times and high selectivity. The ability to tailor the porous structure of LIG through laser processing allows for optimization of sensor performance based on specific application requirements [45]. Another promising application of porous LIG is in environmental monitoring. The unique properties of LIG enable its use in devices designed to detect pollutants in air and water. The porous structure enhances the adsorption of harmful substances, allowing for more efficient detection and quantification. Additionally, LIG can be functionalized to improve selectivity towards specific contaminants, further enhancing its utility in environmental applications [46].

Sensors vary in terms of sensing applications and one type that can be benefitted by LIG, is pressure sensors, which are essential for tactile sensing and artificial intelligence applications. These sensors are frequently manufactured as electronic bandages, enabling the monitoring of physiological parameters. The most commonly employed pressure sensors are piezoresistive sensors, which operate on the principle of varying resistivity in response to applied stress. In contrast, strain gauges function by measuring changes in resistance resulting from alterations in the geometry of the sensor itself. They operate on the principle that the electrical resistance of a conductor changes when it is stretched or compressed. Typically, they consist of a thin metallic foil arranged in a specific pattern and attached to a flexible backing material. When the object being tested deforms, the strain gauge also deforms, resulting in a change in its electrical resistance. This change is directly proportional to the strain experienced by the object, enabling the calculation of stress, torque, pressure, and other mechanical parameters Piezoresistive sensors are particularly advantageous in medical applications due to their sensitivity and ability to provide real-time data on

physiological conditions, making them suitable for use in wearable health monitoring devices [47], [48]. In addition to their role in tactile sensing, pressure sensors are used in robotics for providing feedback on touch and pressure, enhancing the interaction between machines and humans. A resistive pressure sensor has an active layer that is conducive for measurement and elastic for response to pressure, which can be made by coating the conductive nanomaterial [49].

Optical sensors, also referred to as photodetectors, are a category of physical sensors that transform light energy into electrical signals by detecting photons. These sensors have become increasingly significant in optoelectronic applications [50]. LIG has been utilized as lateral electrodes in photodetectors for effective signal collection, attributed to its cost-effectiveness, scalability, and rapid fabrication process, making it a promising candidate for the mass production of optoelectronic devices. Furthermore, LIG-based lateral electrodes contribute to a reduction in the overall thickness of photodetectors, which results in decreased strain and enhanced flexibility. In a study by Qu et al [51], a mass-producible optical sensor was developed using perovskite as the light-sensitive material and LIG as the contact electrodes. The LIG electrodes, created from polyimide via a photothermal laser process, were combined with formamidinium cesium lead triiodide perovskite to form a composite with lateral LIG electrodes. The resulting photodetector demonstrated high conductivity, flexibility, and a strong interface with the perovskite, achieving a broad operational bandwidth of 365 to 940 nm. It also exhibited a responsivity of 15.1 mA W^{-1} and a response time of 0.4 seconds. These findings suggest that LIG could effectively replace noble metal electrodes in optoelectronic applications, offering a more scalable and feasible alternative for mass production [42].

2.3 Laser Gaussian Beams

One type of beam laser sources emit, is the Gaussian beam. The name is derived by the intensity distribution of the beam on the axis of propagation, which is well characterized and its evolution is smooth and easily predictable [52].

Unlike linear optics, focusing of a gaussian beam is characterized by a waist, meaning the beam radius *w(z)* is at its lowest value w_0 *[53]*. As the beam propagates, it experiences divergence in terms of field component amplitudes, wavefront curvature and spot radius. Assuming propagation of a laser beam on the *z-axis*, with $z = 0$ being the focal plane where $w(z) = w_0$, there is a distance extending on either side of $z = 0$, called Rayleigh range (z_R) of the gaussian beam, and describes the negligible divergence of the beam in this range (***Figure 2.5a***).

At z = ± z_R, the radius of the beam is $w(z_R) = \sqrt{2}\, w_0$. The divergence of the beam along z depends on the waist w_0 and the photon wavelength λ *[52]*:

2.5
$$z_R = \frac{\pi w_0^2}{\lambda}$$

This relation can be used for simplification of the dependence of the width, radius of curvature and divergence angle θ, on w_0 and λ [52], [53], [54], [55], [56]:

2.6
$$w(z) = w_0 \sqrt{1 + \left(\frac{z}{z_R}\right)^2}$$

2.7
$$R(z)=z\left[1+\left(\frac{z_R}{z}\right)^2\right]$$

2.8
$$\theta=\frac{\lambda}{\pi w_0}$$

The wavefront at z = 0 is plane and as z increases, so does the radius of curvature, meaning the wavefront is distorted and becomes spherical. The divergence θ, describes the spreading of the beam as it propagates towards infinity [52]. The propagation of the electric field along the z-axis is given by [52], [53], [54], [55], [56]:

2.9
$$E(r,z)=E_0\frac{w_0}{w(r)}\exp\left(\frac{-r^2}{w(z)^2}\right)\exp\left(i\left[kz-\arctan\frac{z}{z_R}+\frac{kr^2}{2R(z)}\right]\right)$$

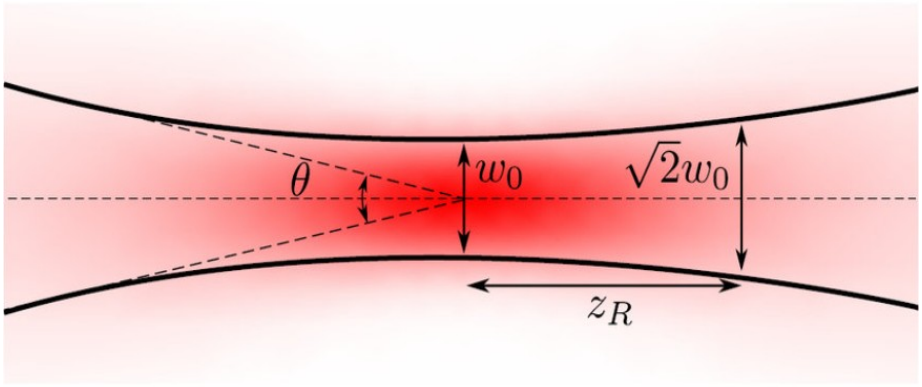
with E_0 the peak amplitude at z = 0 and k = 2π/λ the wavenumber.

The intensity of the beam along the propagation will be given by the simplified equation [52], [53]:

2.10
$$I(r,z)=I_0\exp\left(-2\frac{r^2}{w(z)^2}\right)$$

with I_0 the peak intensity at w(z) = w_0, and the plot of this equation along z is shown in ***Figure 2.5b***. This form of the intensity equation and the plot is convenient for the w_0 of any laser beam at the focal point. Using a CCD camera to determine the laser spot of the beam, and the resulting gaussian intensity plot, the width at the focus can be found. From *Eq.* ***2.10***, the width can be found by the intensity value of $1/e^2$ of the peak Intensity amplitude. Another definition for the beam width at the focus is the Full-Width at Half-Maximum (FWHM) (*Figure 2.5b*) [52], [53].

(a)



(b)

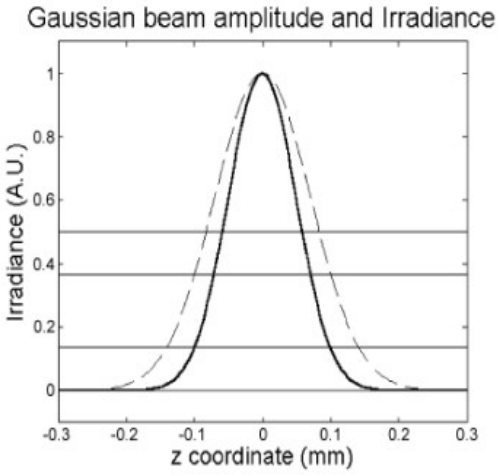


Figure 2.5: (a) *Gaussian beam focus showing w_0 corresponding to z = 0, the Rayleigh range, the divergence θ as well as the intensity along the propagation direction [57]* ***(b)*** *Gaussian beam intensity distribution along the z-axis. The horizontal lines from bottom to top, represent the $1/e^2$, 1/e, and the FWHM values of the peak intensity [52].*

CHAPTER 3

Experimental Methods

This chapter is organized into four distinct sections, each focusing on critical aspects of the experimental methodology employed to achieve LIG patterns on polyimide (PI) substrates using a picosecond fiber laser. The first section provides an overview of the picosecond fiber laser utilized in this study, detailing its operational parameters. These parameters were systematically varied and analyzed to identify the optimal conditions for laser induction on the PI substrate. Additionally, this section includes a description of the laser system and the optical setup, highlighting the use of two distinct optical configurations to enhance the quality of the fabricated LIG. The second section describes the characterization methods used to determine LIG properties. This includes an in-depth analysis using Scanning Electron Microscopy (SEM), Raman spectroscopy, and current-voltage (I-V) measurements to evaluate the structural and electrical properties of the LIG. Through these techniques, we aim to provide a comprehensive understanding of the characteristics and performance of the LIG patterns produced in this study. Finally, the third section describes the optical setups used for the fabrication and optimization of LIG.

3.1 Laser Source

An IPG Ytterbium Picosecond Fiber Laser, operating at wavelength of 1064 nm, was employed for the LIG formation experiments. The laser is a monolithic device that employs high-power semiconductor diodes to pump an active optical fiber, which serves as both the gain medium and the optical resonator. The active fiber core is doped with ytterbium ions, which are responsible for the laser's light amplification. Light emitted from the semiconductor diodes is injected into the cladding of the active gain fiber. This pump light undergoes multiple reflections within the fiber cladding, frequently intersecting the fiber core. As the pump light interacts with the ytterbium ions, it excites them, leading to stimulated emission of light at the laser's operating wavelength of 1064 nm. The picosecond operation of the laser is achieved through the use of specialized techniques that create ultrashort pulses. These pulses are significantly shorter than those produced by traditional nanosecond lasers, allowing for precise material processing with minimal thermal effects. The short pulse duration enables non-thermal absorption of energy [58], [59].

In this type of laser system the laser parameters that it is possible to set are the power, the frequency, which defined the length of the period, the pulse width, that defined the number of the pulses inside the period and the repetition. The laser is pulsed with variable pulse durations ranging from 150 ps to 5 ns (150ps, 1ns, 2ns and 5ns), pulse duration 2-200 kHz and power 10-100% (0.10-30 Watts) approximately. The all fiber format allows for the adjustment of pulse energy and/ or pulse repetition rate without affecting any of the output beam parameters. It is possible to write a

meandrous pattern, where the distance between the lines must be chosen and defined as hatching (dy) expressed in mm. The overall shape is square, with equal width and length.

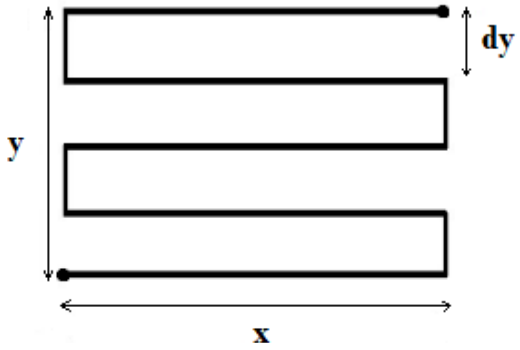


Figure 3.1. *LIG meandrous pattern. The variable dy defines the hatching, y the length, and x the width of the sample*

The choice of a pulsed picosecond fiber laser operating at 1064 nm for fabricating LIG on PI substrates was driven by its ability to achieve precise control over the energy delivery during the fabrication process. This wavelength effectively interacts with the PI material, facilitating efficient carbonization while preserving the integrity of the substrate. The rapid pulse duration allows for localized heating, which is essential for transforming the polymer into a high-quality graphene structure without significant thermal damage.

3.2 Characterization techniques

3.2.1 Electrical measurements

Sheet resistance (R_S) was used as the figure of merit to analyze conductivity, as it is a commonly used measure of resistance, especially for thin films of uniform thickness. This metric allows for the comparison of devices with different sizes. To measure the resistance of a LIG square sample, a Keithley 4200A-ScS Parameter Analyzer was used with two dots of silver paint placed at the edges of the sample. Two co-linear electrical probes, symmetrically positioned on the square samples, were used to measure the resistance. Voltage was swept from -V to V, and the corresponding current values were extracted. The sheet resistance was then calculated using the equation:

3.1
$$R_S = \frac{W}{L} * R$$

where R is the Resistance, W is the Width and L is the length of the sample.

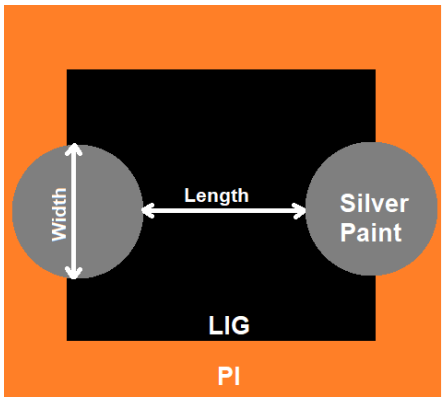


Figure 3.5. *LIG electrical mesurements schematic.*

3.2.2 Scanning Electron Microscopy (SEM)

Analysis of SEM images is a common method of optical characterization of samples in any study, as it provides detailed images with resolution down to the nm-scale. Operation of such microscopes begins with electron extraction from the “electron gun”, typically a wire or tip of metal such as Tungsten, by the application of electricity of thousands of Volts. The extracted electrons are converged with the help of magnetic lenses and apertures, to form an electron beam that is guided on the sample, which is then scanned in a rectangular raster pattern. Upon interaction of electrons with the material, they are scattered, or can induce secondary electrons, which are electrons removed by the sample. The back-scattered and secondary electrons are then collected by detectors, that measure their signals, and map them as variations in brightness in the image display. SEM is used to determine the surface morphology of materials and is a non-destructive measurement method.

In order to characterize the morphology of our LIG samples, and determine the impact of laser fluence on the structure, SEM images were taken, using the JSM-IT700HR High-Resolution Scanning Microscope. This analysis is crucial to optically compare and observe the surface and cross section of samples and perform an initial comparison of quality.

3.2.3 Raman Spectroscopy

Raman Spectroscopy is a crucial tool in characterizing the structure and quality of materials, and especially graphene-related ones. Measurements require a probe laser source and photodetectors that collect the intensity of photons. Incident photons on the material, with certain wavelength and energy, interact with the oscillations of atoms and bonds, and are inelastically scattered at different energies, depending on the energy of the vibrational mode they encountered. The photodetectors measure the intensity of the scattered photons, resulting in the characteristic form of the Raman spectrum, which presents several peaks, according to the material.

In graphene, the Raman spectrum exhibits three distinct peaks, that serve as an indicator of its quality. The D peak (1350 cm^{-1}) corresponds to the breathing modes of sp^2 atoms and is activated by defects, indicating the presence of structural imperfections in the graphene lattice [60]. The G peak (1580 cm^{-1}) is attributed to the in-plane vibrations of sp^2 carbon atoms and is present in all graphitic materials [61]. The 2D peak (2700 cm^{-1}) represents the second order of the D peak and is intrinsic to graphene [61], [62]. The Raman spectrum of LIG is very similar to that of graphene, showing the similarity of the structures, and the justified term of Laser Induced Graphene.

LIG’s quality can be more easily understood through peak intensity ratios. The I_D/I_G ratio reflects the level of disorder within the graphene structure, with lower values indicating higher quality and fewer defects. Studies have shown that this ratio can vary based on laser processing parameters, such as power and pulse duration. A smaller I_D compared to I_G typically signifies a higher degree of structural order, suggesting a substantial amount of sp^2-bonded carbon and fewer defects. For instance, studies on LIG synthesized on PI substrates have shown prominent G peaks, indicating high sp^2 bonding and low defect density. Specifically, Kwak et al. reported I_D/I_G ratios around 0.79 for LIG samples fabricated under lower fluence conditions with a CO_2 laser (1064 nm), implying a multilayer structure with relatively low disorder [63]. The 2D peak represents a specific vibrational mode in carbon-based materials. A taller 2D peak in samples fabricated with lower

fluence indicates better arrangement of sp^2 bonding structures [64]. The ratio to the G peak, I_{2D}/I_G, which compares the intensity of the 2D peak to the G peak, serves as an indicator of the number of graphene layers. A higher I_{2D}/I_G ratio generally signifies better quality graphene, leading to reduced scattering of charge carriers and enhanced mobility and conductivity [65]. LIG samples with a higher I_{2D}/I_G ratio have demonstrated approximately 30% lower sheet resistance compared to pristine LIG, indicating superior electrical conductivity [66].

In this study, a continious wave (CW) laser source was selected to emit at 532 nm wavelength and Raman spectra were extracted for several samples, for the quantified quality form the peak ratios.

3.3 Optical Setups

3.3.1 First Setup (3D Printer stage)

To fabricate laser-induced graphene (LIG), a custom setup was developed by integrating a commercial Ender-3 3D printer as a motion stage and motor-driven galvanic mirrors to steer the laser beam through a lens above the 3D printer's bed. A custom LabVIEW software was used to control the entire system. Despite the high resolution at relatively high speed and low cost, the system did not offer a very high accuracy due to vibrations and not very high precision as the laser beam diameter is bigger than the second optical setup.

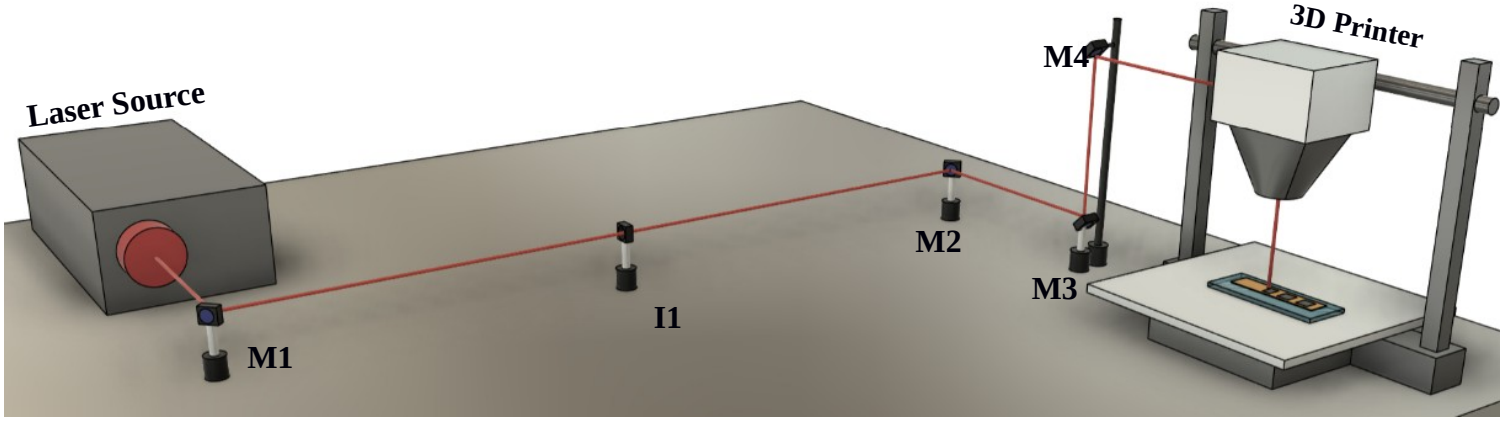


Figure 3.4. *Schematic of the optical setup including 4 Mirrors (M), 1 Iris (I) and a 3D printer's bed as a xy linear stage.*

To determine the optimal focus, the sample was irradiated at varying heights and low laser power, and the laser spot diameter was measured under an optical microscope using ImageJ software, which was found to be 31 μm.

3.3.2 Second Setup (Dedicated XY stage)

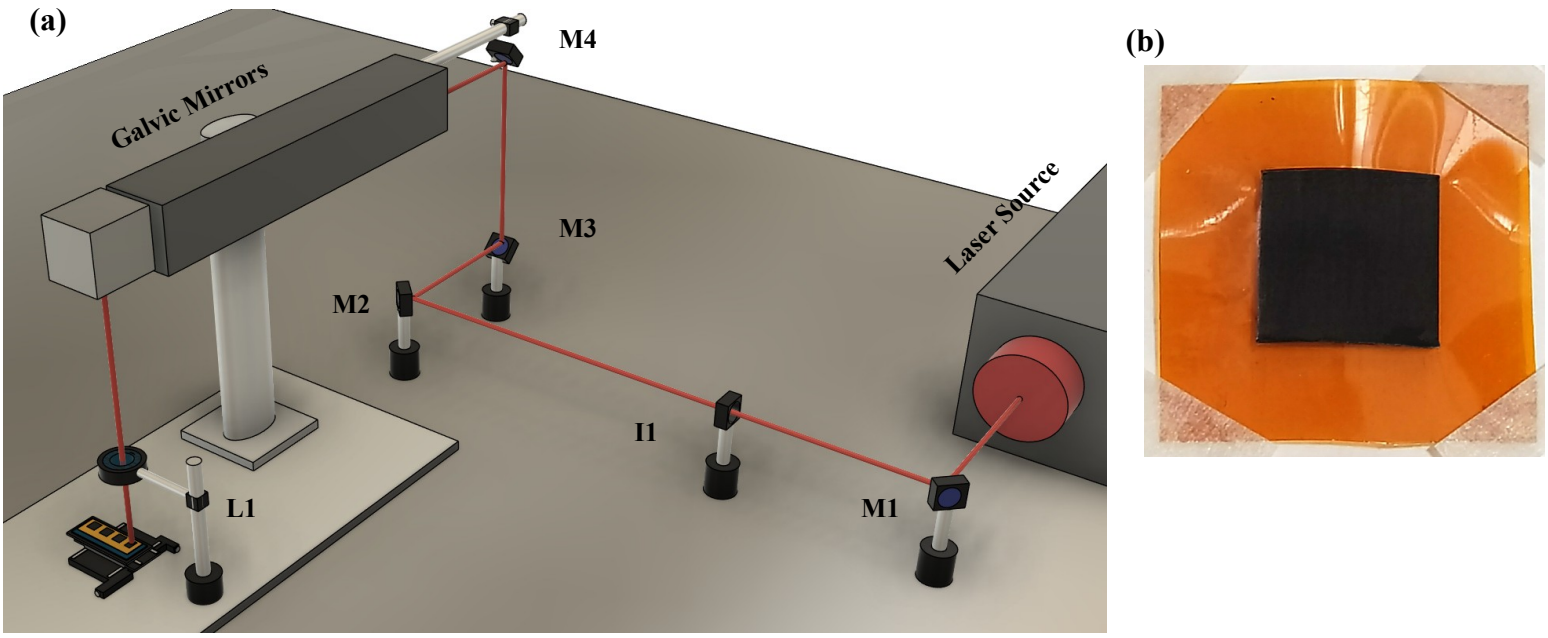


***Figure 3.8**: **(a)** Scheme of the optical setup including 4 Mirrors (M), 1 Iris (I) and 1 Lens (L) of 150 mm. **(b)** LIG sample on PI substrate.*

The second setup employed for the fabrication of LIG was meticulously designed to enhance control over the fabrication process. A Linear Motor Positioning Stage (model 8MT167-25BS1) was utilized to achieve precise positioning of the sample, facilitating the creation of a meandrous LIG pattern using a plano-convex lens with focal length of 150 mm. The laser spot size was determined to be 26 µm through beam profiling, a critical parameter for ensuring accurate material processing.

3.4 LIG in Hydrogen Generation

3.4.1 Hydrogen Evolution Reaction

The application of LIG on polyimide for hydrogen generation presents a promising avenue in the pursuit of sustainable energy solutions. As the demand for clean energy sources intensifies, LIG's exceptional properties, such as high electrical conductivity and large surface area, make it an ideal candidate for enhancing the efficiency of the hydrogen evolution reaction (HER) [67]. The hydrogen generation process utilizing LIG as a catalyst for water splitting involves several key mechanisms that enhance the efficiency of the HER. In this experimental setup, LIG facilitates the electrochemical conversion of water into hydrogen gas through the reduction of protons (H^+) at its catalytic sites. The unique properties of LIG, including its high conductivity and large surface area, play a crucial role in optimizing this reaction [68], [69].

By allowing for the tuning of the material's sheet resistance, LIG enhances charge transfer efficiency during the HER, which is essential for improving hydrogen production rates. The process begins with the absorption of light by the system, which excites electrons and generates charge carriers that migrate to the catalytic sites on the LIG surface. This leads to the reduction of protons, ultimately resulting in the formation of molecular hydrogen (H_2) [70], [71], [72].

3.4.2 Porphyrin functionalization

The integration of porphyrins into the hydrogen generation process enhances the efficiency of the HER due to their unique chemical properties. Porphyrins are well-known as effective photosensitizers, capable of absorbing light and facilitating charge transfer, which is crucial for catalyzing the reaction that produces hydrogen from water. Their molecular structure allows for easy modification, enabling the tuning of their electronic properties to optimize light absorption and enhance photocatalytic activity. In this context, porphyrins can be functionalized with various metal ions, which not only increases the number of active sites available for the HER but also improves the stability and efficiency of the catalytic process. This makes porphyrins particularly suitable for use in hybrid systems, where they can work synergistically with materials like LIG, to achieve lower sheet resistance and improved charge transport, ultimately leading to more effective hydrogen production. The combination of LIG and porphyrins represents a promising strategy for advancing the development of sustainable hydrogen generation technologies [73].

The experimental investigation focused on the combination of LIG with cobalt(II) tetraphenylporphyrin (CoTPP) and copper(II) tetraphenylporphyrin (CuTPP) as catalysts for electrocatalytic hydrogen evolution. These metalic porphyrins were selected due to their proven efficacy and stability in promoting hydrogen production, particularly CoTPP, which has been extensively studied for its high catalytic activity in the HER. The LIG as a substrate serves a dual purpose, acting as both a catalytic surface and a scaffold for the porphyrin molecules, facilitating effective interaction during the electrocatalytic process.

The functionalization of the LIG substrate with cobalt(II) tetraphenylporphyrin (CoTPP) molecular catalyst was carried out using the following procedure, as illustrated in **Figure 3.9**. The LIG sample was secured onto a spin coater using a double-sided carbon tape. The sample was then spun at a rotational speed of 2000 rpm, and a solution of CoTPP in tetrahydrofuran (THF) with a concentration of 1 mg/mL was drop-casted onto the spinning LIG surface in five aliquots of 20 µL each. The resulting functionalized LIG electrodes were subjected to characterization using Raman spectroscopy and SEM.

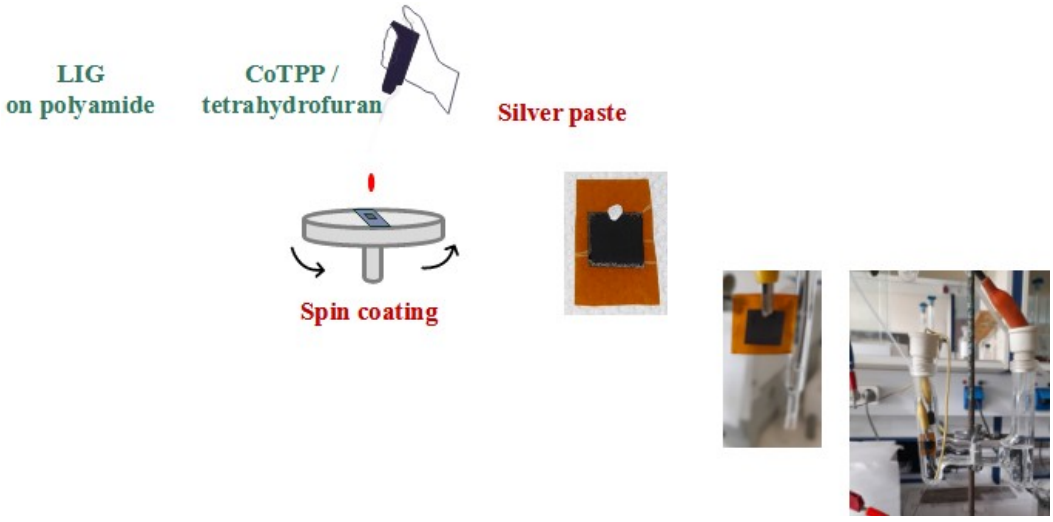


Figure 3.9. *Schematic illustration of the functionalization of LIG substrate with additional molecular catalyst for electrocatalytic hydrogen generation from water.*

3.4.3 HER efficiency measurement methods

The electrocatalytic performance of LIG and porphyrin-functionalized LIG towards the HER was assessed using linear sweep voltammetry (LSV) and chronoamperometry (CA) techniques. The experiments were conducted in a standard three-electrode electrochemical system, with the LIG samples (working area of 1 cm^2) serving as the working electrode, a platinum wire as the counter electrode, and Ag/AgCl as the reference electrode. The HER electrocatalysis was carried out in a 1 M NaOH electrolytic solution purged with N_2 gas. Three sets of samples were tested with sheet resistances 84 Ω/sq (1^{st} set), 84 Ω/sq (2^{nd} set), 16 Ω/sq (3^{rd} set). To investigate the catalytic activity of the prepared samples towards HER, linear sweep voltammograms were recorded in the potential window of 0 to -1.5 V vs. Ag/AgCl at a sweep rate of 5 mV/s.

To assess the stability of the catalysts, which is a crucial parameter for their potential commercial application, the prepared samples were subjected to chronoamperometric measurements. The stability was studied using the CA technique for a duration of 1 minute by applying a constant potential of -0.6 V vs. Ag/AgCl.

CHAPTER 4

Results & Discussion

This chapter presents the results of the experimental LIG optimization, and their subsequent characterization and quality determination, as well as the performance of our LIG samples, both pure, and functionalized with porphyrins, in hydrogen generation. Moreover, a comparison of the electrical properties of the samples is presented, to highlight the satisfying results of our study.

4.1 Laser Characterization

To investigate the relationship between the laser output power and the power percentage set in the laser software, a series of measurements were conducted while maintaining a constant repetition rate of 60 kHz. The power percentage was incrementally increased from 10% to 90% in 10% steps for pulse durations of 1 ns, 2 ns, 5 ns, and 150 ps. The output power was measured using a power meter, and the values were plotted to generate graphs for each pulse width.

The resulting plots exhibit a linear relationship between the power percentage and the output power for all four pulse widths. This linear trend can be attributed to the direct proportionality between input power and output power, as described by the laser rate equations. Notably, the slope of the linear plot for the 150 ps pulse width was the smallest among the four, followed by the slopes for 1 ns, 2 ns, and 5 ns pulse widths. It is important to note that the repetition rate of 60 kHz represents the minimum value that could be set for a pulse width of 150 ps, while the minimum allowable repetition rate for the other three pulse widths was 2 kHz.

This phenomenon can be explained by the concept of peak power, which is the maximum optical power attained during a pulse. Shorter pulse durations, such as 150 ps, result in higher peak powers because the same amount of energy is concentrated in a shorter time frame.

The relationship can be expressed mathematically as follows [74]:

$$Peak\ Power = \frac{Pulse\ Energy}{Repetition\ Rate * Pulse\ Width} \tag{4.1}$$

The smaller slope for the 150 ps pulse width indicates that the output power increases less significantly with increasing power percentage compared to longer pulse widths. In contrast, longer pulse widths (1 ns, 2 ns, and 5 ns) exhibit similar slopes that are larger than that of the 150 ps pulse width, suggesting that the system operates more linearly over the range of power percentages tested. This behavior underscores the significance of pulse duration in optimizing laser output power and efficiency [75].

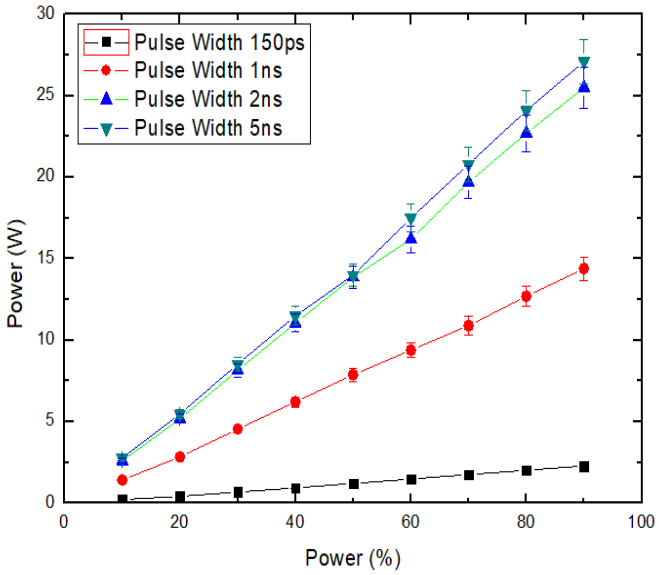


***Figure 4.1**: Laser Power output for stable repetition rate (60 kHz) and varying pulsed widths.*

4.1.1 Humidity and lasers

Humidity significantly impacts the stability and performance of laser systems, particularly in controlled laboratory environments. Fluctuations in humidity levels can cause variations in laser output power, as moisture in the air alters the refractive index of the medium through which the laser beam propagates. This change can lead to instability in the laser beam characteristics, resulting in inconsistent performance during experiments. Studies have shown that changes in relative humidity critically affect laser pulse energy, influencing both high and low fluence outputs, which can compromise the precision of laser applications. Additionally, high humidity can cause condensation on optical components, further degrading the quality of the laser output. Therefore, maintaining stable humidity levels is essential for ensuring reliable laser operation and achieving consistent results in experimental applications [76].

The interaction between humidity and polyimide (PI) substrates is crucial in understanding their performance in various applications. PI is known to be hydroscopic, meaning it can absorb moisture from the environment. This absorption can lead to significant changes in the physical and optical properties of the material, including alterations in thermal conductivity, dielectric constant, and mechanical strength. As humidity levels increase, the moisture absorbed by the PI can also affect its dimensional stability, potentially leading to warping or other structural changes. Research indicates that changes in relative humidity can result in design specification violations concerning dimensional requirements in materials like PI, particularly in additive manufacturing processes. These variations can influence the interaction between the PI substrate and external stimuli, such as laser light, thereby affecting the overall performance and reliability of devices that utilize PI. Consequently, controlling humidity is vital for maintaining the integrity and functionality of PI substrates in experimental and industrial applications [77].

Temperature is a critical factor that significantly influences the output power and overall performance of laser systems. As the temperature of the laser diode increases, several physical phenomena can lead to a decrease in output power. Elevated temperatures can cause a shift in the laser's emission wavelength, resulting in reduced efficiency and stability of the laser output. Specifically, the increase in temperature can lead to a higher threshold current required for lasing, thereby diminishing the output power at a given input current. Additionally, thermal effects can

induce changes in the refractive index of the gain medium, which can further affect the beam quality and stability. The relationship between laser output power and ambient conditions can be illustrated in the following graph. When effective thermal management strategies are implemented, such as the utilization of heat sinks, active cooling systems, and rigorous temperature monitoring, the laser output power remains stable across varying ambient conditions. This stability underscores the critical role of thermal management in maintaining optimal laser performance and ensuring consistent operational results [78].

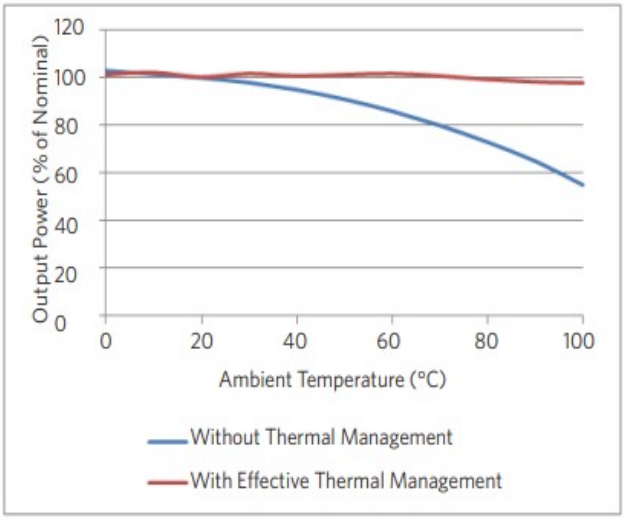


***Figure 4.2**: Impact of the effective thermal management on output power. [78]*

4.2 LIG Optimization & Characterization

4.2.1 First Setup (3D Printer Stage)

The primary objective of this research was to identify the optimal parameters for fabricating high-quality LIG with superior electrical conductivity. The approach involved varying one parameter while keeping the others constant and then measuring the sheet resistance of the samples.

The first step was to determine the optimal pulse duration among 1 ns, 2 ns, and 5 ns. As shown in ***Figure 4.3a***, the 1 ns pulse duration exhibited the lowest sheet resistance when the repetition rate and fluence were kept constant. Subsequently, different fluences were tested while maintaining a steady repetition rate and pulse duration, revealing the best fluence to be 23.3 J/cm^2 ***Figure 4.3b***. In addition to pulse duration and fluence, the hatching distance, defined as the spacing between adjacent laser lines, was also varied to optimize the quality of the LIG. The analysis indicated that a hatching distance of 31 μm yielded the best results, as demonstrated in the graph ***Figure 4.3c***. This optimal spacing of the laser beam scanning allows for adequate overlap of the laser-induced areas, enhancing the overall conductivity of the LIG. Finally, the fluence and pulse duration were held constant, and the repetition rate was varied. ***Figure 4.3d*** indicates that the optimal repetition rate is 80 kHz. By systematically optimizing these key parameters—including pulse duration, fluence, hatching distance, and repetition rate—the conductivity of the fabricated LIG can be significantly improved, paving the way for its use in various applications that require high-performance graphene-based materials.

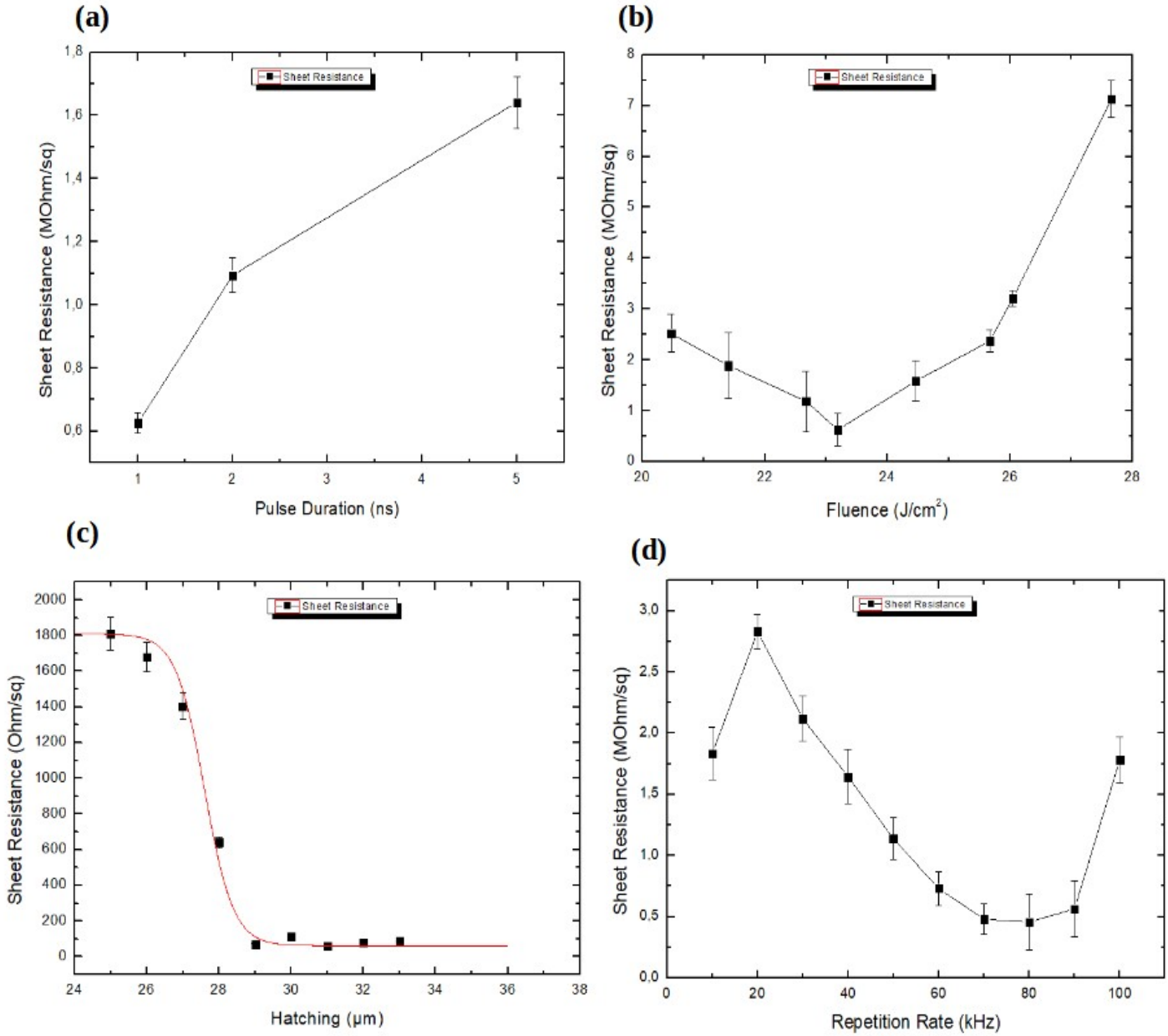


Figure 4.3. ***(a)*** *Pulse Duration- Sheet Resistance plot for LIG samples fabricated with 23.2 J/cm^2 and 10kHz,* ***(b)*** *Fluence- Sheet Resistance plot for LIG samples fabricated with 1ns and 10 kHz,* ***(c)*** *Hatching dy- Sheet Resistance plot for LIG samples fabricated with 150ps, 1.9 W, 4.4 J/cm^2,70 kHz and z=1.76 mm,* ***(d)****Repetition Rate- Sheet Resistance plot for LIG samples fabricated with 23.2 J/cm^2 and 1ns.*

In addition, the distance between the galvic mirrors and the 3D printer's bed's home position was altered. Thermal degradation of the samples was observed at distances z=1.74mm and 1.78mm, surrounding the critical point at z=1.76mm. Analysis reveals that the midpoint, situated at z=1.76mm, corresponds to the focal point within the Rayleigh range. At focal point the sheet resistance was equal to 84 Ohm/sq, keeping the other parameters at the ideal values that were presented above.

This analysis was performed on the sample exhibiting the lowest sheet resistance within this experimental setup. The SEM images revealed a distinctly uniform and porous morphology of the LIG. However, challenges arose during the examination of other samples due to their higher resistance values, which were elevated due to the incomplete transformation of PI to LIG and the insulating properties of the PI substrate. To mitigate charging artifacts during imaging, the

deposition of a gold (Au) layer onto the material's surface was performed, prior to SEM characterization. In particular, SEM images of samples fabricated with a lower laser power of 1.6 W (3.7 J/cm^2) displayed a non-uniform surface, characterized by regions exhibiting a porous morphology indicative of LIG, alongside areas where the polyimide had not induced into graphene. In contrast, SEM images obtained at a higher laser power of 1.9 W (4.4 J/cm^2) demonstrated a significantly more uniform surface, with complete transformation of the polyimide into LIG. The resulting morphology was characterized by a porous texture, with distinct laser-etched lines clearly visible across the sample. Furthermore, cross-sectional analysis conducted using ImageJ software revealed that the thickness of the LIG layer measured approximately 40.2 ± 10.4 μm (due to thickness fluctuations, ***Figures 4.4ghi***). This comprehensive characterization related to the influence of laser power on the morphological properties of LIG, highlighting the importance of optimizing fabrication parameters to achieve uniform and high-quality graphene structures.

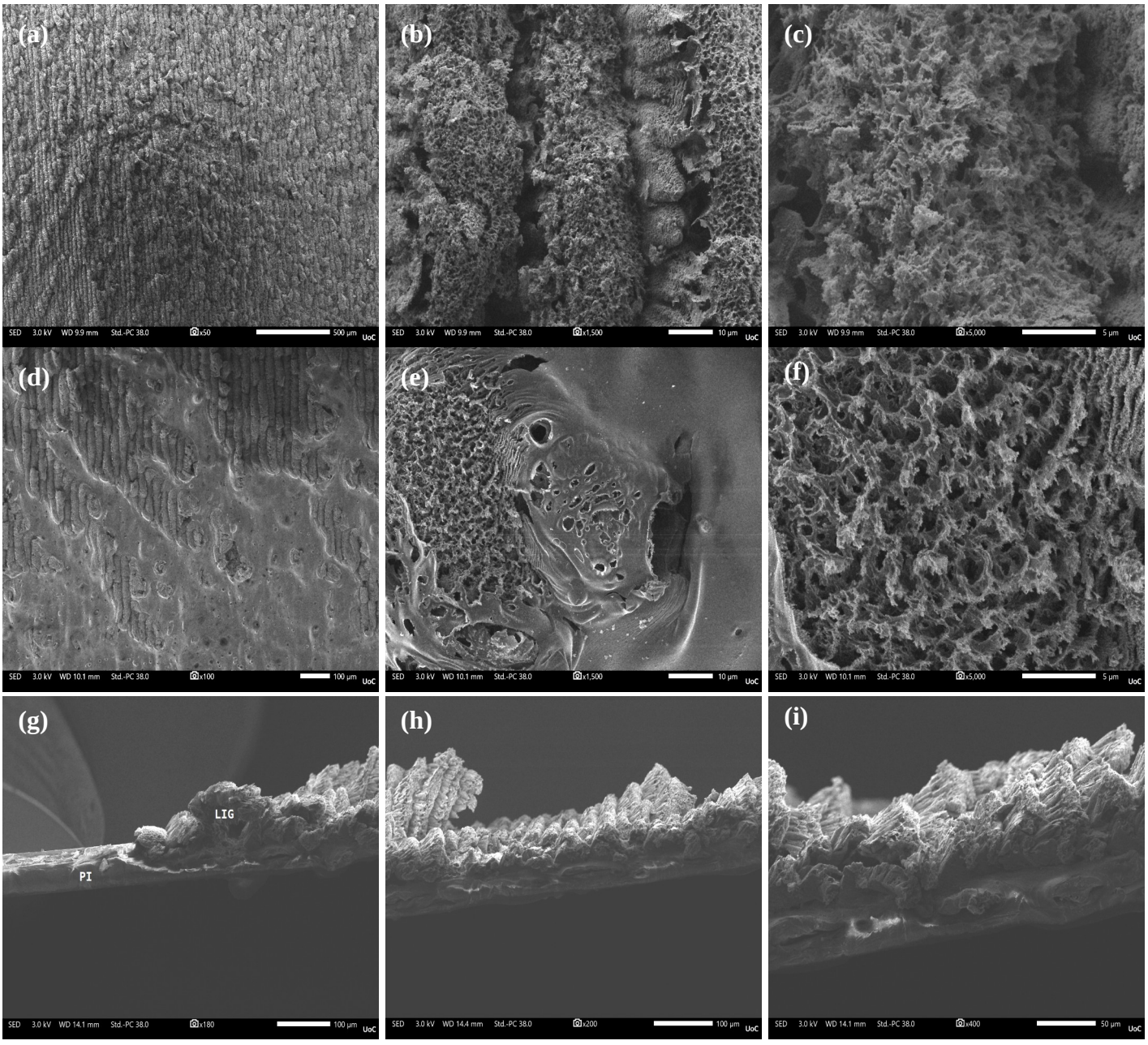


Figure 4.4. *LIG formation under ambient conditions.* ***(a)*** *Top view SEM image of LIG fabricated with power 1.9W (4.4 J/cm^2), 70 kHz, Magnification x50,* ***(b)*** *Top view SEM image of (a), Magnification x1500,* ***(c)*** *Top view SEM image of (a), Magnification x5000,* ***(d)*** *Top view SEM image of LIG fabricated with power 1.6W (3.7 J/cm^2), 70 kHz, Magnification x50,* ***(e)*** *Top view SEM image of (d) fabricated with power 1.6 W (3.7 J/cm^2), 70 kHz, Magnification x1500,* ***(f)*** *Top view SEM image of (d) fabricated with power 1.6W (3.7 J/cm^2), 70kHz, Magnification x5000,* ***(g)*** *Cross section of LIG fabricated with power 1.9 W (4.4 J/cm^2), 70 kHz, Magnification x150,* ***(h)*** *Cross section of LIG fabricated with power 1.9 W (4.4 J/cm^2), 70 kHz, Magnification x200,* ***(i)*** Cross section of LIG fabricated with power 1.9 W (4.4 J/cm^2), 70kHz, Magnification x400.

4.2.2 Second Setup (Dedicated XY Stage)

The meandrous pattern provided tunability in the dimensions of the final sample and the hatching distance (dy), which was optimized at 28 µm for effective LIG fabrication. The scanning speed of the stage was set at 5 mm/s, allowing for controlled movement during laser application. A pulse duration of 150 ps was selected for this setup, significantly shorter than the nanosecond (ns) pulse durations commonly used in LIG fabrication. The use of shorter pulse durations results in higher peak power, which enhances energy concentration at the focal point. This increased energy density promotes efficient ablation of the polyimide substrate, leading to a more effective conversion to graphene. Additionally, the rapid energy delivery minimizes the heat-affected zone, thereby reducing thermal diffusion into the surrounding material and preserving the integrity of the substrate. The ultrafast nature of the 150 ps pulses further facilitates precise control over the material removal process, which is essential for achieving high-quality LIG patterns with desirable electrical conductivity [46], [79].

Upon interaction with the polyimide substrate, the laser beam generates localized plasma due to the high energy density at the focal point. This plasma is pivotal in the ablation process, aiding in the conversion of polyimide to graphene. The optimized hatching distance of 28 µm ensures effective interaction between the plasma generated by one laser pulse and the subsequent pulse, preventing excessive overlap that could induce undesirable thermal effects or damage [80].

Following this fabrication process, the resistances of each sample were measured using a Keithley 4200A-SCS Parameter Analyzer, applying the appropriate formula for resistance determination. The sheet resistance of the LIG was significantly influenced by variations in laser process parameters. Specifically, achieving high-quality conductive films required precise laser fluence. As illustrated in ***Figure 4.5a***, the sheet resistance decreased with increasing fluence, reaching a minimum value of 16 Ω/sq at a fluence of 0.59 J/cm². This value is notably lower than the 36.6 Ω/sq reported by Sartanavičius et al. [81], indicating further optimization of the laser processing parameters. Beyond this optimal fluence, the sheet resistance began to increase, suggesting a threshold beyond which the quality of the conductive film deteriorates due to defects induced by excessive thermal effects [82].

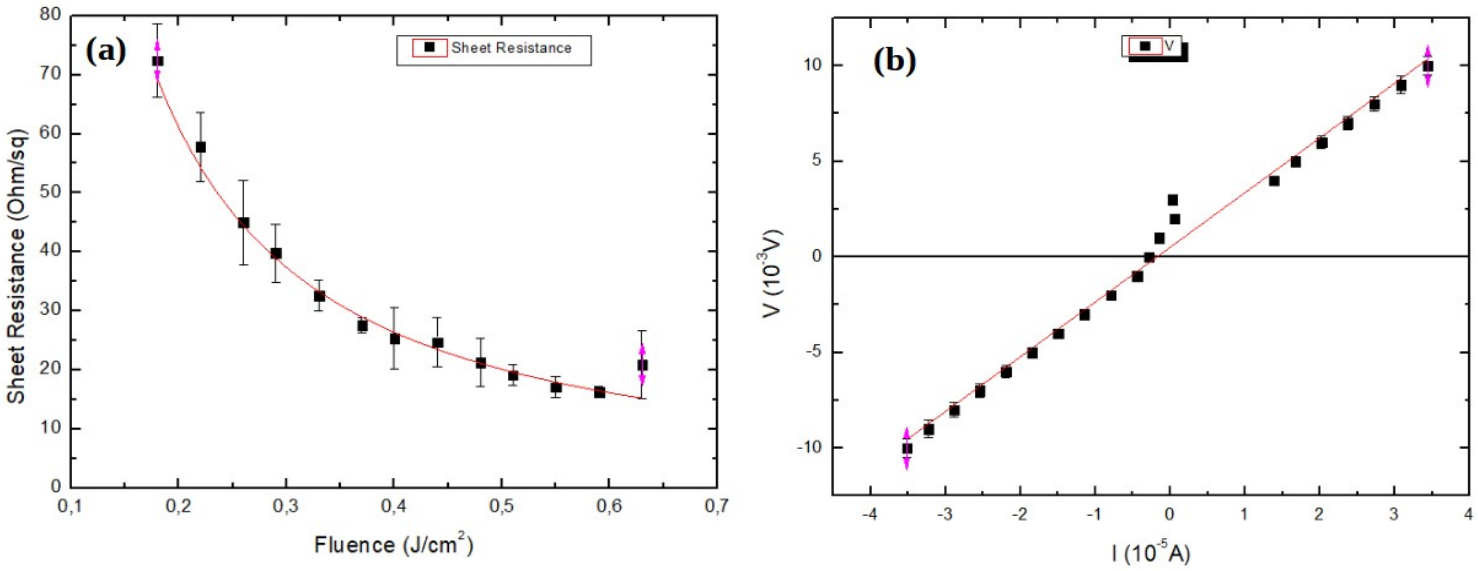


***Figure 4.5**: **(a)** Dependence of the electrical sheet resistance [Ohm/sq] to fluence [J/cm²] **(b)** I-V plot example of LIG sample*

Figure 4.5b illustrates the I-V plot of the LIG sample, demonstrating a linear increase in current with increasing voltage. This linear relationship indicates that the LIG sample exhibits ohmic behavior, conforming to Ohm's law. The linear I-V dependence suggests that the LIG sample maintains a constant resistance over the measured voltage range, with the slope of the line representing the conductance of the LIG, the inverse of its resistance [83]. Notably, as the measurements were not conducted under absolute darkness, a slight shift in the graph was observed, indicating a change in conductivity due to the generation of electron-hole pairs within the LIG material [84].

SEM images of samples clearly show the porous structure of LIG, which is the result of photothermally induced release of gaseous byproducts [85]. Depending on the ultrashort pulsed beam fluence on the polymer substrate, porosity and surface morphology differ. Notably, the SEM images of sample, with the lowest sheet resistance, fabricated with 0.26 J/ cm^2 (***Figure 4.6a, c***) and sample fabricated with 0.56 J/cm^2 (***Figure 4.6b, d***) fluence, exhibit highly different surfaces. The sample fabricated with lower fluence, is characterized by a surface lacking porosity, whereas the higher fluence sample has a highly porous surface, with large pore size. In the case of 0.26 J/cm^2, the fluence is insufficient to effectively break C-N and C-O bonds and to ionize the released gasses, resulting in an incomplete transformation of PI to LIG. Increasing the fluence, will result in efficient bond breaking, with subsequent gas ionization and localized temperature increase, which results in higher quality porous LIG. Cross-sectional SEM images of the samples (***Figures 4.6c, f***), confirm the presence of porosity on the LIG sample, with thickness measuring 74 ± 5 μm and 120 ± 10 μm, respectively. ***Figure 4.6d*** reveals a secondary layer of LIG, characterized by a distinct texture, situated between the surface LIG and the polyimide (PI) substrate. This phenomenon occurs due to insufficient laser fluence, which fails to penetrate through the entire substrate, thereby preventing the formation of a uniform LIG layer throughout the material.

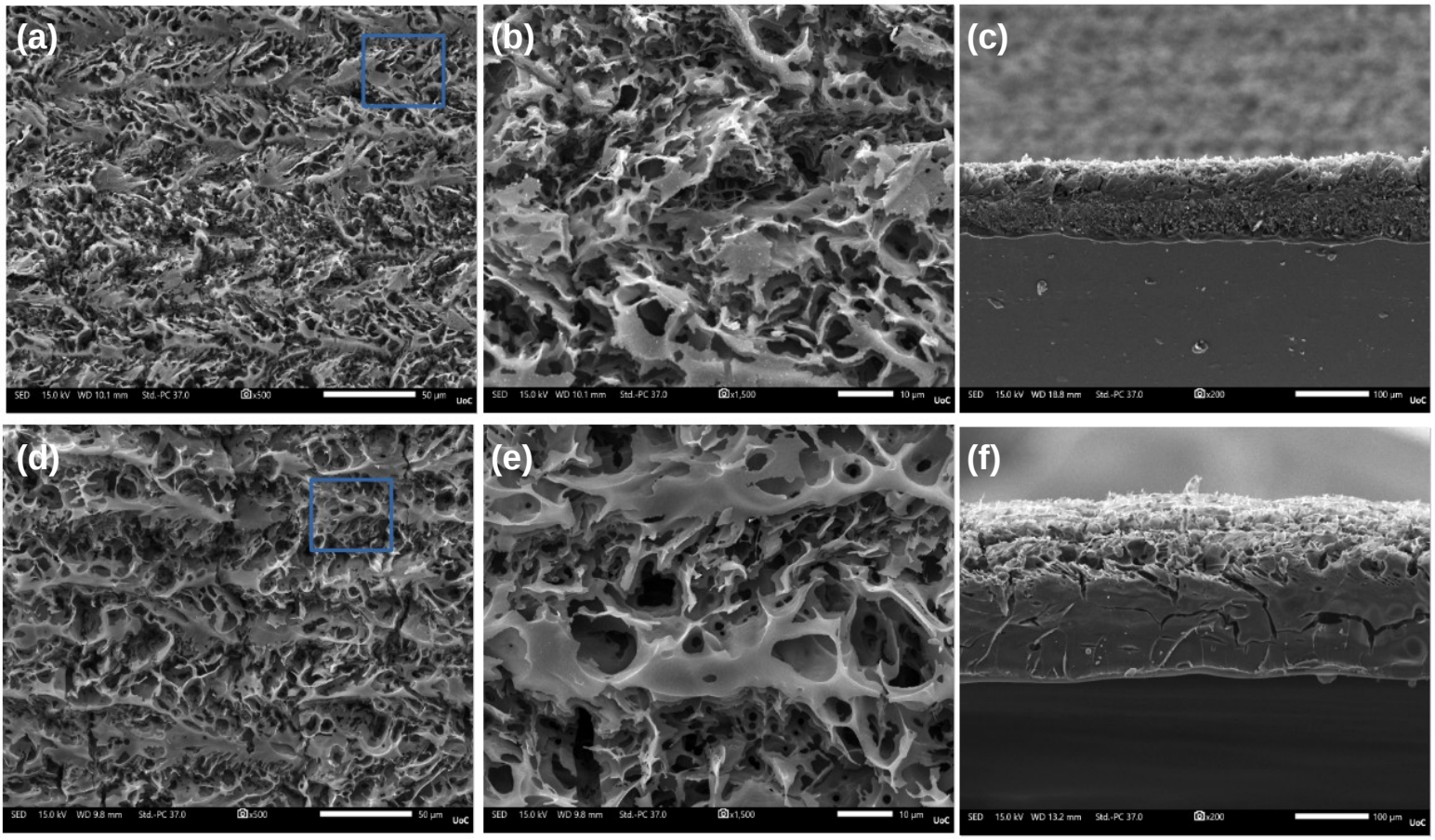


Figure 4.6: *LIG formation under ambient conditions.* ***(a)*** *Top view SEM image of LIG fabricated with fluence of 0.26 J/cm^2, Magnification x500,* ***(b)*** *Top view SEM image of (a), Magnification x1500,* ***(c)*** *Cross section SEM image of (a), Magnification x200,* ***(d)*** *Top view SEM image of LIG fabricated with fluence of 0.59 J/cm^2, Magnification x500,* ***(e)*** *Top view SEM image of (d), Magnification x1500,* ***(f)*** *Cross section SEM image of (d), Magnification x200.*

It is possible to quantify the percentage of PI that is converted to LIG during the laser treatment process, by the cross sectional SEM images. ***Figure 4.6f*** reveals remaining PI of thickness 8.6 μm at the bottom of LIG. The initial thickness of the PI film is 70 μm. Laser treatment of a 1×1 cm^2 PI sample produces the final product of ***Figure 4.6f***, with volumes of PI before and after treatment:

4.2

$$V = Width \cdot Length \cdot Thickness = 2.52 \cdot 10^{-3} cm^3 \text{ before treatment}$$

$$V' = 0.31 \cdot 10^{-3} cm^3 \text{ after treatment}$$

From the maker's data sheet for the PI film, its density is given as 1.42 g/cm^3 [86], which can be used to determine the mass of PI:

4.3

$$m = \rho \cdot V = 3.58 \cdot 10^{-3} g$$

$$m' = \rho \cdot V' = 0.44 \cdot 10^{-3} g$$

So the total mass of PI that was converted to LIG is 3.14 mg, meaning the theoretical conversion percentage of PI to LIG is 87.7%. This percentage describes the amount of LIG that is formed on a PI sheet, assuming all PI mass affected by the laser is converted to LIG. However, that is not the case in practical LIG generation, as part of PI is released from the material in the form of gas, which is responsible for the materials porosity.

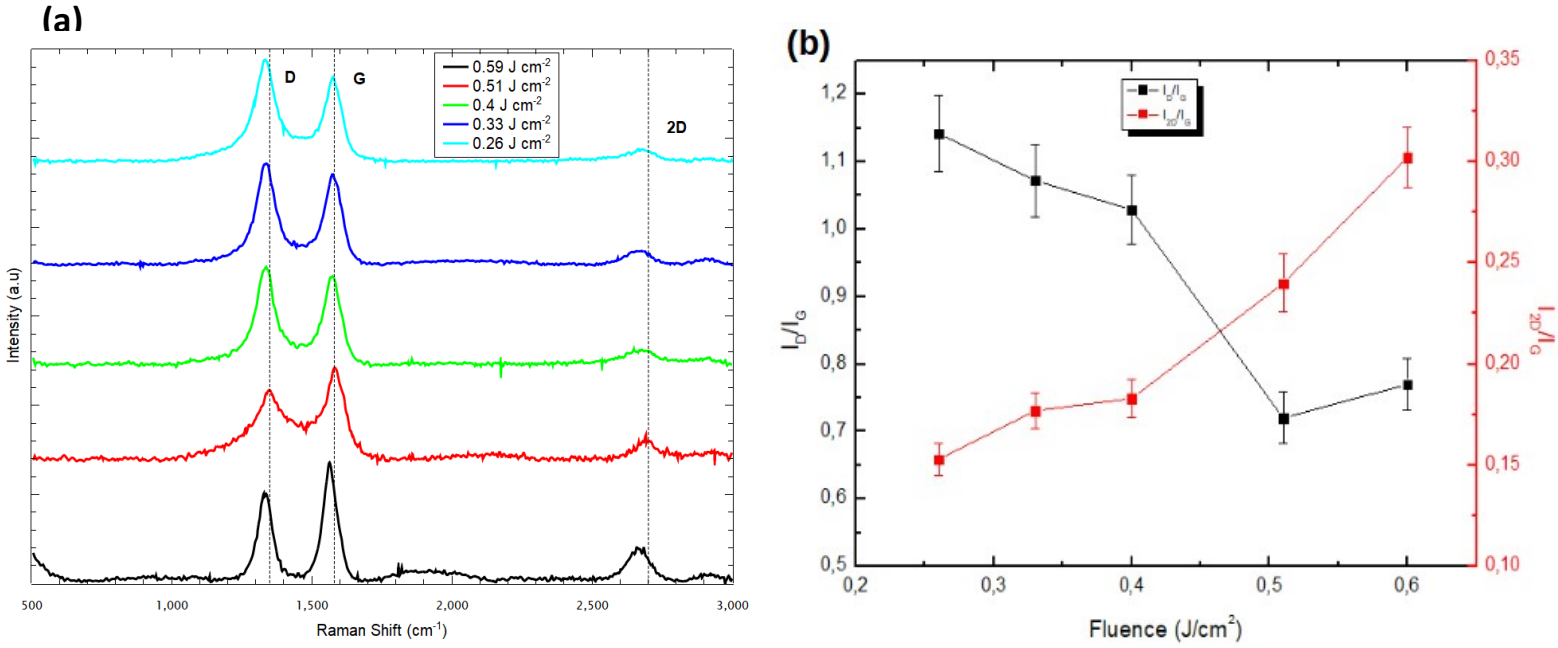
To determine the percentages of converted PI mass, a 6x6 mm^2 LIG sample (***Figure 4.6f***) and a 6x6 mm^2 pristine PI film were weighted on a KERN ABT 320-4NM scale. The values for the weights are 2.1 mg for the PI and 1.8 mg for the LIG sample with 8.6 µm PI remaining. The volume of the remaining PI under the LIG can be found by the ***expression 4.2***, at 0.0003096 cm^3, which can be used together with PI's density to find its mass through ***expression 4.3***. The mass of the remaining PI amounts to 0.44 mg. The mass of PI can now be found by:

$$m_{total} = m_{LIG} + m_{PI} \Rightarrow m_{LIG} = m_{total} - m_{PI} = 1.36\,mg$$

So the actual weight percentage of PI converted to LIG will be 1.36 mg/ 2.1 mg, or 64.76%.

Figure 4.7a illustrates the Raman spectra of five samples prepared at different fluences, (0.26,0.33,0.4,0.51 and 0.59 J/cm^2), highlighting the prominent peak characteristics of graphene. As the laser power increases, both the intensity and half-width of these characteristic peaks exhibit variations, but the Raman shift remains unchanged, with negligible shift, that is attributed to slightly different energy levels of vibrational modes [87], originating from laser processing. The intensity ratios I_D/I_G and I_{2D}/I_G of LIG prepared at different powers indicate variations in defect density and carbon atom stacking of graphene as a function of laser fluence (***Figure 4.7b***). The sample fabricated with fluence 0.26 J/cm^2, exhibited the highest I_D/I_G ratio, ~1.14, indicating a higher level of defects. As fluence increases, the I_D/I_G ratio decreases, while the I_{2D}/I_G ratio increases, suggesting a reduction in structural defects [88].

Notably, the sample fabricated with fluence 0.51 J/cm^2, exhibits a slightly lower I_D/I_G ratio of 0.72, in contrast with the sample fabricated with 0.59 J/cm^2 which shows an I_D/I_G of 0.77 and a I_{2D}/I_G ratio of 0.3, indicating superior material quality. Higher I_{2D}/I_G ratios are an indicator of enhanced graphenization and improved stacking of graphene layers, whereas lower ratios suggest the presence of alternative carbon forms, such as amorphous carbon, resulting from fluctuations in laser power during the fabrication process [89].



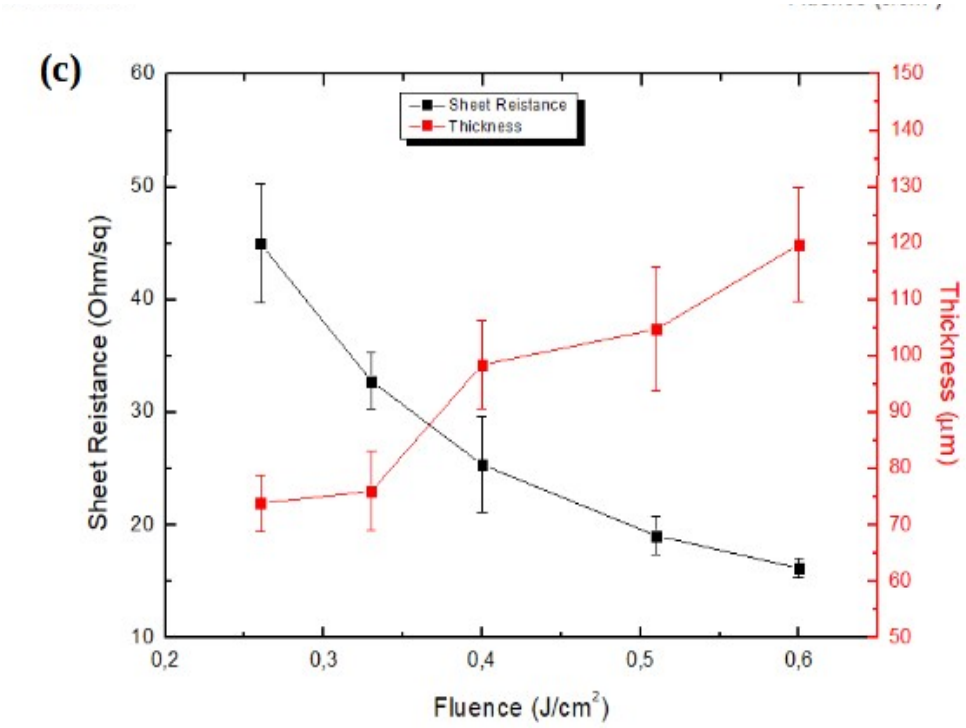


Figure 4.7. (a) *Raman Spectra of 5 LIG samples* ***(b)*** *Intensity ratio of peaks in (a) as a function of fluence.* ***(c)*** *Influence of Fluence on the Sheet Resistance and Thickness of LIG Samples.*

The sheet resistance of LIG was notably influenced by changes in the laser process parameters. Specifically, the formation of LIG required a precise laser fluence to produce a high-quality conductive film. As illustrated in ***Figure 4.5a***, the sheet resistance decreased with increasing fluence, achieving a minimum value of 16 Ω/sq at a fluence of 0.59 J/cm². This value is lower compared to the 36.6 Ohm/sq reported by *Sartanavičius, A. et. al.[81]*, underscoring the further optimization of laser processing parameters. Beyond this optimal point, the sheet resistance increased again, indicating a threshold beyond which the quality of the conductive film deteriorates, due to higher fluences inducing defects originating from thermal effects [82]. These results are consistent with the SEM and Raman analysis of samples, where the highest quality LIG was shown to be fabricated at 0.59 J/cm^2. The samples at lower fluences exhibit increased sheet resistance due to lower quality graphene, characterized by defects and surface inhomogeneity. Higher quality porous films show better conductivity due to their uniform structure, which facilitates efficient charge transfer across the material.

The graph in ***Figure 4.7c*** demonstrates how varying fluence affects the sheet resistance and thickness of five LIG samples produced on a polyimide substrate. As the fluence is increased, the thickness of the samples increases reaching ~120 µm, for the highest quality sample. The data suggest that optimizing fluence for LIG fabrication on PI significantly influences material properties, with higher fluences resulting in thicker, more conductive layers, due to better graphenization of the whole PI film.

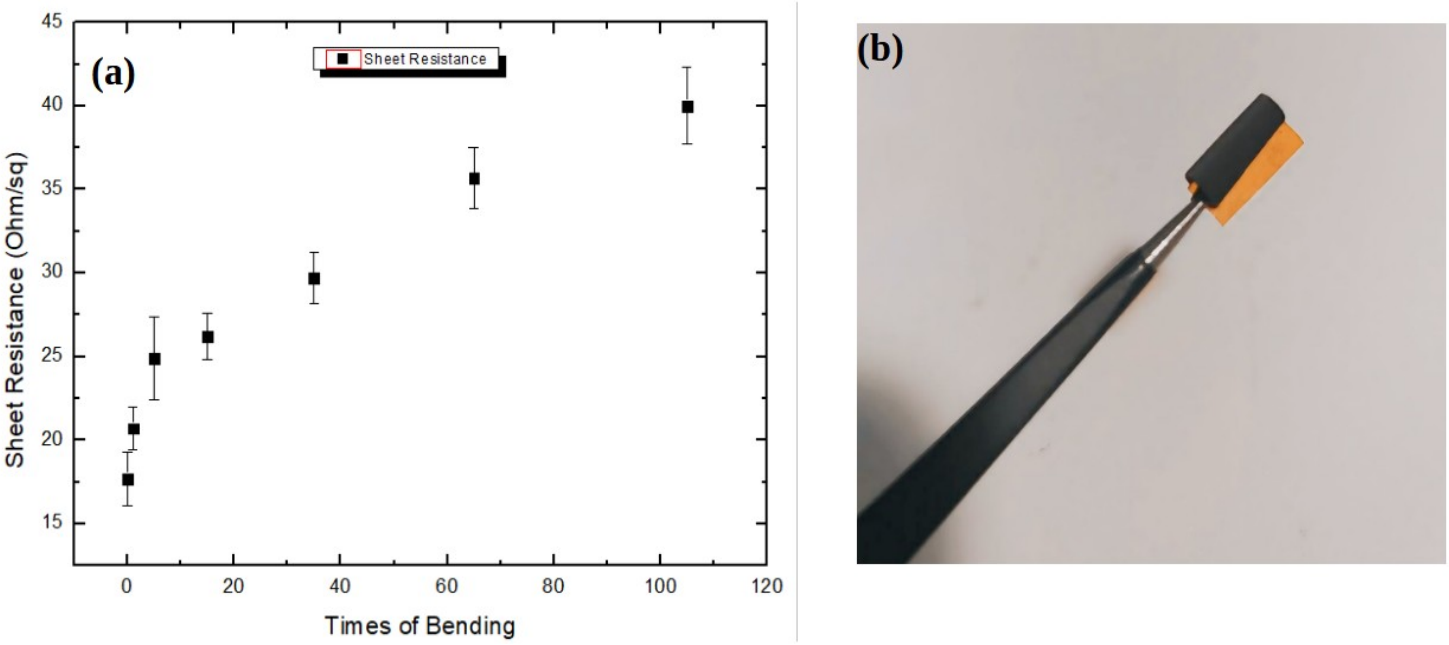


Figure 4.8. ***(a)*** *Flexibility test plot of the sample fabricated with 0.6 J/cm^2 fluence and 1x1 cm dimentions.* ***(b)*** LIG sample fully bent forming a complete circle.

The flexibility of LIG is a critical factor for its potential applications in flexible electronics and wearable devices. To evaluate this property, a series of systematic flexibility tests were conducted, wherein a square LIG sample was subjected to repeated folding. The primary objective of this experiment was to assess the impact of mechanical deformation on the electrical resistance of the LIG material. Specifically, the sample was folded multiple times at predetermined intervals—1, 5, 15, 35, 65, and 105 folds—and the corresponding resistance was measured after each folding cycle with a multimeter. The plot (***Figure 4.8a***) demonstrates the sample's ability to withstand mechanical deformation without significantly compromising its electrical properties. Although a notable increase in sheet resistance was observed after 100 bending cycles, with values rising from an initial measurement of 17 Ohms to nearly 40 Ohms, it is important to highlight that no visible changes in the material were detected, both macroscopically and microscopically. Visual inspections and microscopic examinations revealed that the structural integrity of the LIG samples remained intact, exhibiting no signs of delamination, cracking, or other forms of mechanical degradation. This observation suggests that repeated mechanical stress may affect the electrical properties of the material. However, the overall physical structure of the LIG retains its robustness, indicating a degree of resilience that is critical for applications in flexible electronics.

4.3 Comparison of State-of-the-Art LIG from different laser types

Different Laser types have different impact on polymeric substrates, inducing various reactions and thus LIG fabrication is extensively affected. Femtosecond lasers, characterized by pulse durations on the order of 10^{-15} seconds, represent a significant advancement in laser technology, enabling the creation of high-quality microstructures with minimum thermal damage to surrounding materials. In the study conducted by Wang et al. (2024), femtosecond laser direct writing technology was employed to fabricate multiscale hybrid-structured femtosecond laser-induced graphene (FsLIG) on polyimide substrates in ambient air. The sheet resistance of the FsLIG was measured at approximately 18.2 Ω/sq, significantly enhancing its electrothermal conversion performance [90]. Femtosecond laser pulses generate localized heating due to their high peak power and short duration, causing the polymer chains in polyimide to break down and rearrange into a

graphene-like structure. The resulting FsLIG exhibits a high light absorption rate of approximately 98.5% across a broad spectrum (220–1400 nm), which enhances its ability to convert light into heat. Additionally, the low sheet resistance of FsLIG allows for efficient electrical conduction; when an electric field is applied, the material generates heat through Joule heating, further enhancing its thermal performance. This dual capability enables the material to respond effectively to both light and electrical stimuli, making it particularly suitable for applications such as anti-icing and deicing. The transformation from polyimide to graphene involves significant alterations in chemical bonding and the arrangement of carbon atoms, with the intense energy from femtosecond laser pulses facilitating the formation of sp^2 hybridized carbon structures characteristic of graphene while simultaneously removing functional groups that may inhibit conductivity [91]. The ultrashort pulse duration of picosecond lasers minimizes thermal damage while enabling effective photomechanical interactions that shatter target materials into smaller particles, making them suitable for applications in high-frequency electronic devices and flexible electronics.

In contrast, picosecond lasers, with pulse durations ranging from 1 to 100 picoseconds, offer a balance between precision and efficiency, though femtosecond lasers provide even greater precision due to their shorter pulse durations. Picosecond lasers operate through both photothermal and photomechanical mechanisms, allowing for effective carbonization while minimizing thermal diffusion, leading to a more controlled formation of LIG. Research by Sartanavičius et al. demonstrated that a picosecond laser (1064 nm) was used to create a conductive graphene network within a PI matrix, resulting in a sheet resistance of approximately 36.6 Ω/sq, as confirmed by Raman spectroscopy. [81].

Nanosecond lasers typically induce thermal and photothermal reactions due to their longer pulse durations, which allow for significant thermal diffusion and extensive heating of the substrate. This heating facilitates carbonization and rearrangement of the polymer chains in polyimide into graphene-like structures; however, this method carries a higher risk of thermal damage compared to ultrafast lasers. Studies indicate that nanosecond laser processing can yield sheet resistances ranging from 16 to 36 Ω/sq depending on specific parameters such as laser power and scanning speed. The longer pulse duration allows for more extensive heating but may lead to greater thermal damage in surrounding areas [62].

UV lasers can initiate both photochemical reactions, such as bond breaking and material ablation, and photothermal effects that result in localized heating. Operating at shorter wavelengths (e.g., 355 nm), UV lasers effectively interact with organic materials like polyimide, breaking chemical bonds through direct photon absorption. As fluence increases, photothermal effects become more pronounced, raising the temperature of the material and leading to thermal expansion or carbonization of the substrate. The combination of photothermal and photochemical effects enhances the efficiency of graphene production, allowing for significant alterations in surface morphology and improved electrical properties [92], [93]. **Table 4.1** compares sheet resistances of LIG resulting from various types of lasers.

Laser Type	Reaction	Sheet resistance	Reference
Nanosecond (CO_2)	thermal and photothermal	16 to 36 Ω/sq (27.4 Ω/sq)	[62], [94]
Picosecond	photothermal and photomechanical	36.6 Ω/sq	[81]
Femtosecond	photo-electo-thermal	18.2 Ω/sq	[90]
UV laser (355 nm)	photothermal and photochemical	20 Ohm/sq	[92]
Our study: Picosecond	photothermal and photomechanical	16 Ohm/sq	This work

Table 4.1. Comparison of different laser types on LIG fabrication.

4.4 LIG as electrodes in Hydrogen Generation

The Raman spectra of the functionalized LIG samples, shown in ***Figure 4.9***, revealed the presence of both LIG-derived and porphyrin-derived bands, with no significant shifts observed. In contrast, SEM analysis, as presented in ***Figure 4.10***, showed notable structural changes. A comparison of Figure 4a and 4b suggests that the tetraphenylporphyrin (TPP) moiety reduces the porosity of the LIG, likely due to the vitrification of TPP molecules within the LIG porous structure. This observation may explain the less distinct Raman spectra obtained from the same sample, as indicated by the red line in ***Figure 4.9***. The incorporation of CoTPP appears to have minimal impact on the LIG structure, as illustrated in ***Figure 4.10c***. However, in the case of copper(II) tetraphenylporphyrin (CuTPP), the formation of octahedral nanostructures on top of the porous LIG was observed.

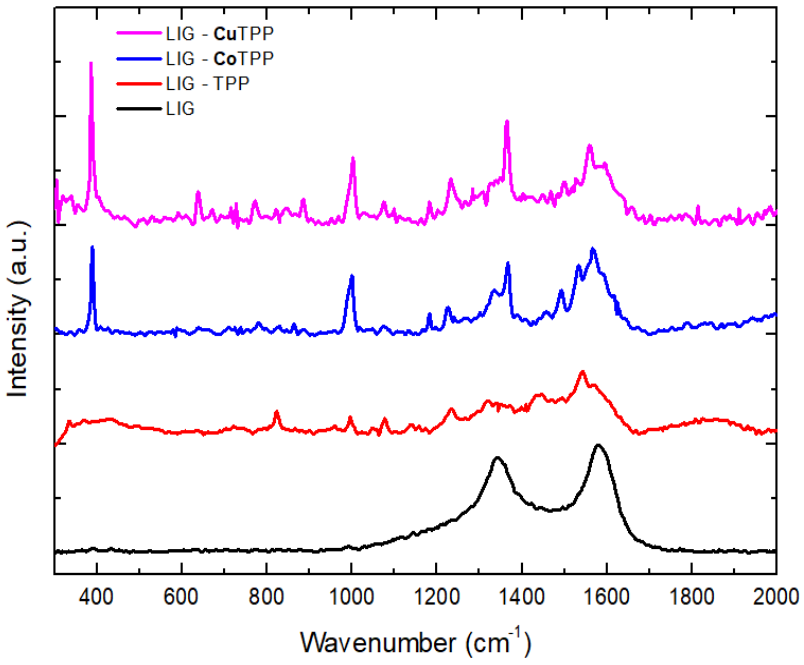


Figure 4.9. *Raman spectra of functionalized LIG substrates.*

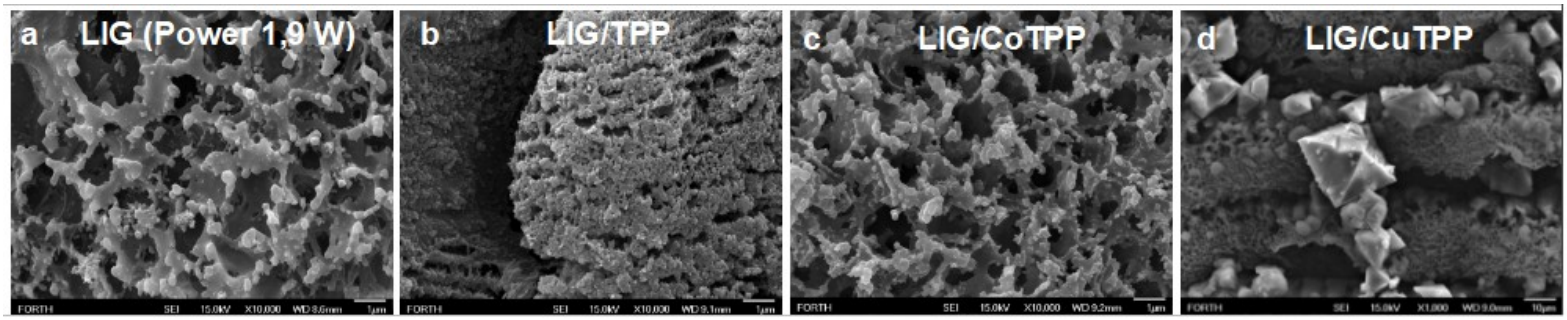


Figure 4.10. *SEM images of functionalized LIG substrates.*

Figure 4.11a,c shows the crhonoamperometry and LSV curves for LIG and reference samples, while ***Figure 4.11b,d*** presents the results for different sets of LIG samples. The findings revealed that the porphyrin-functionalized LIG samples exhibited lower performance compared to the non-functionalized LIG samples. This observation can be attributed to the limited number of available pores in the functionalized samples, which may hinder electron transfer and the proximity of proton cations required for the reaction. Therefore, the investigation continued by focusing on improving the LIG as a working electrode without additional functionalization. Furthermore, the LSV results indicated that the 3rd set of LIG samples demonstrated superior electrochemical performance.

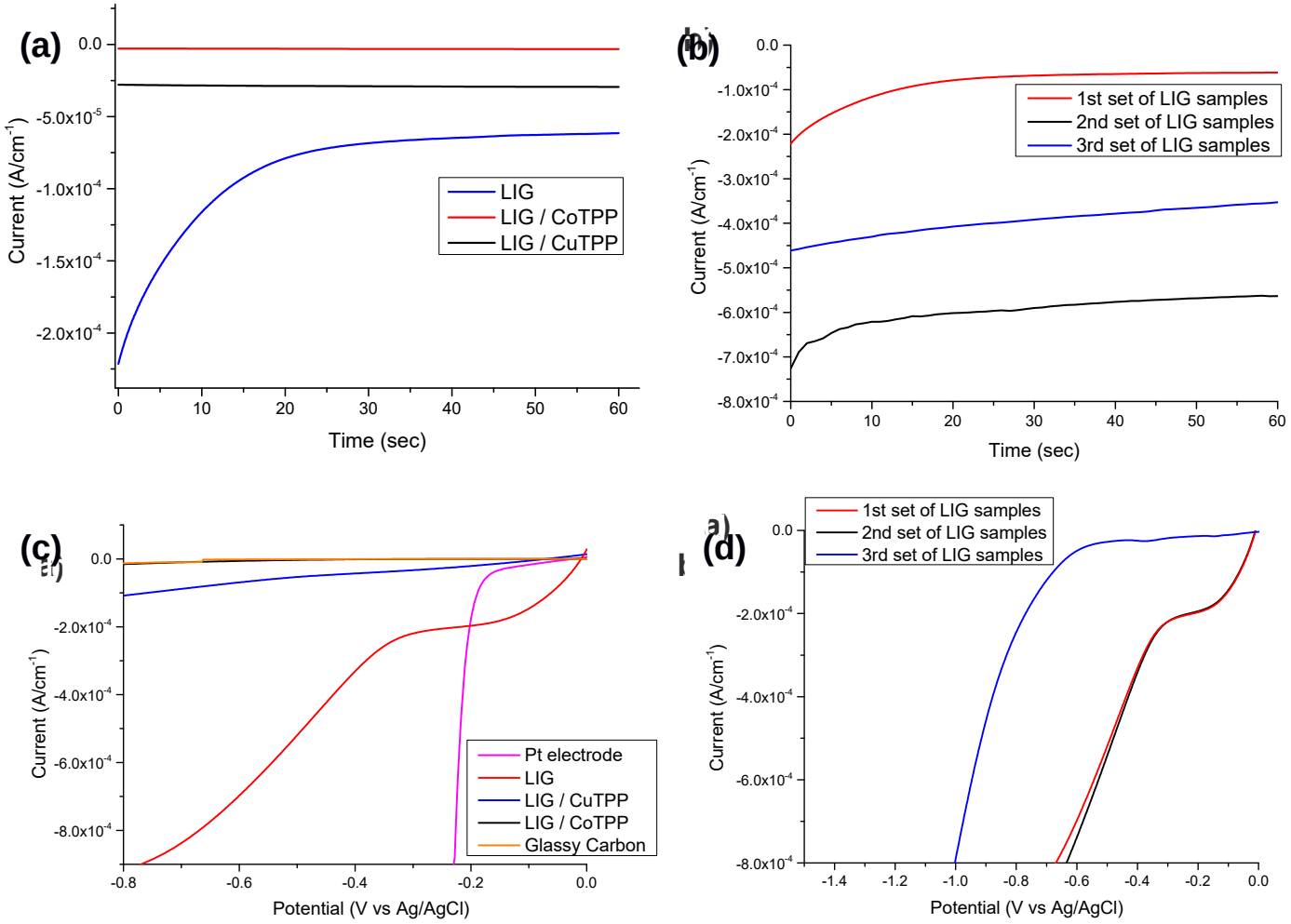


Figure 4.11. (a) *Chronoamperometric (CA) curve investigated for the period of 1 minute at the constant potential −0.6 V vs Ag/AgCl, for LIG and functionalized LIG samples*. ***(b)*** *Chronoamperometric (CA) curve investigated for the period of 1 minute at the constant potential −0.6 V vs Ag/AgCl for different sets of LIG samples.* ***(c)*** *Electrocatalysis of HER – LSV curves recorded for LIG and reference samples.* ***(d)*** *Electrocatalysis of HER – LSV curves recorded for different sets of LIG samples.*

Chronoamperometry measurements were conducted on all samples, as shown in **Figures 4.11a** and **4.11b**. The results clearly indicate that most samples exhibited stability during HER electrocatalysis, as they retained a significant portion of their current density. The results of the first and second set of samples are greatly different, possibly due to humidity effects on the PI and the laser.

In conclusion, the combination of LSV and CA techniques provided valuable insights into the electrocatalytic performance and stability of LIG and porphyrin-functionalized LIG for the hydrogen evolution reaction. The findings suggest that further optimization of the LIG material is necessary to enhance its catalytic efficiency, while the stability analysis confirms the potential of these materials for practical applications in hydrogen generation.

CHAPTER 5

Conclusions

This master thesis investigated the synthesis and application of LIG on PI for electrocatalytic hydrogen generation, among other apllications. Utilizing a picosecond fiber pulsed laser with a wavelength of 1064 nm, LIG was successfully fabricated, achieving an exceptionally low sheet resistance of 16 Ω/sq under ambient conditions. This low sheet resistance is indicative of the high electrical conductivity of the material, which is essential for enhancing the efficiency of electrocatalytic processes. Structural characterization of the samples confirmed the high quality of LIG with the lowest sheet resistance, showing fewer inconsistencies and defects, which further contributes to its superior conductivity. By controlling parameters such as laser pulse duration, fluence, repetition rate, and hatching distance (the spacing between laser patterns), the resulting LIG exhibits minimal defects and a high degree of sp^2 hybridization. This high-quality structure is essential, as it enhances the efficiency of π-π* transitions, where electrons are excited from bonding π orbitals to antibonding π* orbitals, thereby improving charge carrier mobility. In contrast, other studies have reported elevated sheet resistance values, possibly attributed to non-optimal processing conditions that lead to increased defect densities or uneven heating profiles. For example, while some investigations have achieved lower sheet resistance through different laser wavelengths or irradiation techniques, these methods frequently compromise the structural integrity and mechanical stability of produced LIG. The presented optimization not only maintains a low sheet resistance but also ensures robust adhesion to the polyimide substrate, which is vital for practical applications in flexible electronics. Consequently, the combination of advanced processing parameters and the intrinsic properties of graphene, positions the fabricated LIG as a contender to those reported in existing literature. This advancement underscores its potential for innovative applications, particularly in high-performance sensors and electrochemical devices, making it an ideal candidate for hydrogen evolution reactions (HER) due to its enhanced conductivity and structural stability [92], [95], [96], [97].

The remarkable conductivity of LIG underscores its potential as an effective material for various electronic and energy applications. Specifically, the HER was found to be more efficient with pure LIG samples, as functionalization with porphyrins can hinder charge transfer and pore availability, which are critical factors for optimizing catalytic activity. The results indicated that the third set of samples, consisting of LIG with a sheet resistance of 16 Ω/sq, served as the optimal electrode, demonstrating promising performance in HER and stability during chronoamperometry (CA) tests.

While the initial findings were encouraging, further optimization of the LIG material may be required to enhance both HER performance and stability. Additionally, exploring different

porphyrins for functionalization could yield better results compared to the metallic porphyrins tested in this study, potentially improving the overall catalytic efficiency.

Moreover, the porous structure confirmed by SEM images can be employed in water filtration systems for filtering bacteria and large contaminant molecules. To this end, LIG with tailored porosity is required, which contrasts with the focus of this thesis on optimizing the conductivity of the prepared samples.

In summary, this research establishes a foundational understanding of LIG's properties and its application in hydrogen generation, paving the way for future investigations aimed at optimizing its performance. The findings contribute to the broader goal of developing sustainable energy solutions and reducing reliance on fossil fuels, emphasizing the potential of LIG as a versatile and effective material in renewable energy technologies.

CHAPTER 6

Future prospects

6.1 Alternative Substrates

LIG was originally fabricated through the laser treatment of commercial polymers, particularly polyimide and polyetherimide (PEI), which are suitable due to their high content of repeating aromatic or imide units that can be transformed into graphene structures.

Polyimide has emerged as the preferred material for LIG production, as evidenced by the extensive body of literature surrounding its use. Its chemical structure contains hexagonal crystalline carbon and imide groups, and it exhibits excellent photon energy absorption in the infrared and near-ultraviolet regions, allowing for effective laser processing [98], [99]. Polyimide is thermally stable up to 550°C, and during laser irradiation, it undergoes several stages: the release of nitrogen and oxygen gases at 550°C [4], carbonization at 700°C, and graphitization at 3000°C [100].

In terms of mechanical properties, LIG on polyimide demonstrates durability and stability, even after multiple bending cycles, making it suitable for various applications, including on-body point-of-care sensors [101], [102], [103]. However, its stiffness limits its stretchability, which is a critical factor for wearable devices. To address this limitation, a novel technique was developed to transfer LIG from polyimide to polydimethylsiloxane (PDMS) [104], a highly flexible and stretchable elastomer, enabling applications such as strain gauges for detecting finger movement. Additionally, LIG-metal nanomaterial composites on PDMS have been designed for the detection of both electrochemical and physiological parameters in human subjects [105].

Recently, bio-derived materials have emerged as sustainable alternatives to synthetic polymers for LIG precursor substrates. These materials, sourced from raw unprocessed materials like wood, cork, and leaves, or byproducts from wood and paper production, include lignocellulosic materials, cellulose, and lignin [106], [107]. Among these, lignocellulosic materials have shown electrical performance comparable to that of polyimide-derived LIG. Raman spectroscopy results indicate that precursor materials with higher lignin content yield LIG with fewer defects, while those with high cellulose content result in poorer electrical properties. This shift towards bio-derived materials highlights the potential for LIG production to meet industrial and medical application needs while achieving sustainability targets [108].

6.2 Fabrication Process- Nitrogen atmosphere

While this study successfully demonstrated the fabrication of laser-induced graphene (LIG) from polyimide substrates under ambient conditions, the future prospects of this material can be significantly enhanced by conducting the laser treatment in a controlled nitrogen atmosphere. The use of a nitrogen environment has the potential to minimize structural defects and improve the overall quality of the graphene, leading to enhanced electrical and mechanical properties [109], [110].

Nitrogen can effectively passivate edge dangling bonds and defects in graphene, thereby reducing interactions between graphene nanosheets and layers. The lone pair electrons of nitrogen can interact with the π orbitals of graphene, resulting in a π-π conjugation effect. This effect involves a system of connected p-orbitals with delocalized electrons, chatacteristic of compounds with alternating single and multiple bonds. Such interaction helps stabilize the edges and defects, making them less reactive and enhancing the overall electronic properties of the material. Furthermore, nitrogen plasma treatment can incorporate nitrogen atoms into graphene, yielding N-doped graphene with various nitrogen configurations, including pyridinic N, pyrrolic N, and graphitic N [110], [111]. The type and concentration of these nitrogen configurations depend on plasma exposure time and can be evaluated using techniques like X-ray photoelectron spectroscopy (XPS) and near-edge X-ray absorption fine structure (NEXAFS) spectroscopy [109], [112].

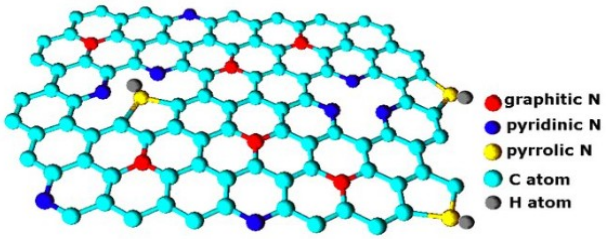


***Figure 6.1**: Bonding configuration of Nitrogen in graphene [113].*

By conducting the laser treatment in a controlled nitrogen environment, it is expected that the resulting LIG will exhibit lower sheet resistance and a more uniform surface, as the risk of oxidation and moisture absorption will be minimized. This enhanced quality of graphene will position it as a more viable material for applications in electronics, energy storage, and flexible devices. Future research should focus on optimizing the nitrogen treatment parameters, such as gas flow rate, pressure, and exposure time, to achieve the best possible outcomes in terms of structural integrity, electrical performance, and mechanical flexibility [109], [114].

LIG can be significantly enhanced by its integration with zinc oxide (ZnO) nanorods, which can lead to improved material properties and broaden its applications. ZnO is a direct wide bandgap semiconductor with a bandgap of 3.37 eV at room temperature and a high exciton binding energy of 60 meV. This allows it to efficiently absorb UV light and generate electron-hole pairs for photocatalytic applications [115].

ZnO has a higher electron mobility compared to other materials like TiO_2 and a tunable morphology, as it can be synthesized in various nanostructures including nanorods, have a high aspect ratio and provide a large surface area for enhanced interaction with the graphene matrix, making it particularly suitable for incorporation into LIG. The one-dimensional (1D) nanorod

structure of ZnO offers several advantages, including improved charge separation due to the effective migration of photoexcited electrons along the axis of the nanostructure, photoexcited electrons migrate along the axis of the nanostructure toward the tip, while holes migrate to the sides. This effective separation of photogenerated charges leads to enhanced photocatalytic activity [116].

In addition the high aspect ratio of ZnO nanorods provides a larger surface area for interaction with the graphene matrix, leading to improved photocatalytic performance and enhanced adsorption capacity. This interaction can result in enhanced photocatalytic activity, due to increased chemical stability, light absorption range and intensity, and improvement of active sites [115]. making LIG modified with ZnO nanorods effective for applications such as the photocatalytic degradation of organic dyes and the development of antibacterial materials [117], [118].

6.3 Applications regarding flexibility

The flexibility and lightweight nature of LIG on PI substrates make it an ideal candidate for applications in flexible and wearable electronics. According to this study and previous flexibility test has been demonstrated the exceptional flexibility of LIG, with the material withstanding multiple bending cycles without visible cracking, despite a slight increase in sheet resistance. This indicates that the material can endure mechanical stress while retaining its conductive properties, which is vital for wearable applications where the device must conform to various surfaces and withstand daily use.

To further improve the stability of sheet resistance, future research could focus on optimizing the laser parameters, such as pulse duration and energy density, to enhance the uniformity and conductivity of the LIG. Additionally, incorporating additives or using composite materials, such as integrating LIG with conductive polymers or metal nanoparticles, could help maintain low sheet resistance while enhancing mechanical properties. Mixing LIG with conductive materials, such as metal nanoparticles or conductive polymers, can create a composite with improved mechanical and electrical properties. For example, a Cu/cellulose paper composite demonstrated excellent flexibility and maintained stable sheet resistance even after 40 folding cycles [119].

Moreover, the introduction of heteroatom doping (e.g., nitrogen or boron) during the fabrication process may also contribute to improved electrical stability and conductivity, as these dopants can create localized electronic states that facilitate charge transport. By focusing on these strategies, the outcome of LIG can be tailored to achieve ideal performance for flexible and wearable electronics, ensuring that sheet resistance remains stable even after extensive mechanical deformation [46].

6.4 Applications regarding porosity

The high porosity of LIG, resulting from its three-dimensional structure, significantly enhances its surface area and accessibility for interactions with other materials. This characteristic is particularly beneficial for applications in energy storage, such as lithium-ion batteries, where the porous structure allows for efficient lithium ion diffusion and enhances the overall electrochemical performance.

Yi et al. laser irradiated PI film on copper foil to obtain an array structure consisting of copper foil, PI column, and LIG. Among them, the copper foil acted as a conductive channel for lateral electrons, the PI pillar relieved the stress generated by Li deposition, and the LIG film acted as a

nucleation site for Li. As a result, this approach allowed the Li-metal anode to achieve a high coulombic efficiency of 99% at 1 mA cm^{-2} and a high cycle life of 400 h [120].

Yang et al. proposed a novel CuS/Cu_2S aqueous solution cell. They used a composite of LIG mixed with sulfur as the cathode of this cell. The large specific surface area of LIG sheets (up to 294.69 m^2 g^{-1}) provided a large number of surface-active sites. Due to the synergistic effect of the new redox couple and LIG, when the current density was 0.8 A g^{-1}, the discharge capacity of the battery reached 1654.7 mAh g^{-1} at the initial cycle. Moreover, 91.2% of the reversible capacity was retained after 328 cycles [121]. So, the high specific surface area of LIG can reduce local current density during lithium deposition, thereby promoting stable cycling and improving coulombic efficiency in lithium-metal anodes [120].

Moreover, the porosity of LIG makes it an excellent candidate for gas sensing applications. The large number of surface-active sites available in the porous structure facilitates gas-solid interactions, allowing for rapid and sensitive detection of various gases. For instance, LIG-based gas sensors have demonstrated fast response times and high sensitivity to gases such as NO_2 and NH_3, making them suitable for environmental monitoring and safety applications [42]. The ability to tailor the porosity of LIG through laser processing parameters further enhances its performance in these applications, allowing for the optimization of sensor characteristics based on specific detection needs. Additionally, the biocompatibility of porous materials opens up avenues for medical applications, such as in tissue engineering and drug delivery systems. The porous structure of LIG can facilitate cell infiltration and nutrient transport, making it a promising candidate for scaffolds in regenerative medicine [122]. The ability to modify the porosity of LIG can help create scaffolds that mimic the natural extracellular matrix, promoting better cell attachment and growth.

Future research should focus on refinement of porosity through laser processing techniques to maximize the benefits in these diverse fields, ultimately contributing to the development of advanced materials for flexible and wearable electronics, environmental monitoring, and medical applications.

References

[1] California Institute of Technology. (n.d.-c). *There's plenty of room at the bottom - Caltech Magazine*. https://calteches.library.caltech.edu/1976/

[2] Novoselov, K. S., Geim, A. K., Morozov, S. V., Jiang, D., Zhang, Y., Dubonos, S. V., Grigorieva, I. V., & Firsov, A. A. (2004a). Electric field effect in atomically thin carbon films. *Science*, *306*(5696), 666–669. https://doi.org/10.1126/science.1102896

[3] P. E. Dyer, M. Pervolaraki, and T. Lippert, "Experimental studies and thermal modelling of 1064- and 532-nm Nd:YVO4 micro-laser ablation of polyimide," *Appl. Phys. A*, vol. 80, no. 3, pp. 529–536, Feb. 2005, doi: 10.1007/s00339-004-3085-0.

[4] J. Lin *et al.*, "Laser-induced porous graphene films from commercial polymers," *Nat. Commun.*, vol. 5, no. 1, p. 5714, Dec. 2014, doi: 10.1038/ncomms6714.

[5] Y. Chen *et al.*, "UV Laser-Induced Polyimide-to-Graphene Conversion: Modeling, Fabrication, and Application," *Small Methods*, vol. 3, no. 10, p. 1900208, 2019, doi: 10.1002/smtd.201900208.

[6] Y. Dong, S. C. Rismiller, and J. Lin, "Molecular dynamic simulation of layered graphene clusters formation from polyimides under extreme conditions," *Carbon*, vol. 104, pp. 47–55, Aug. 2016, doi: 10.1016/j.carbon.2016.03.050.

[7] T.-S. D. Le *et al.*, "Recent Advances in Laser-Induced Graphene: Mechanism, Fabrication, Properties, and Applications in Flexible Electronics," *Adv. Funct. Mater.*, vol. 32, no. 48, p. 2205158, 2022, doi: 10.1002/adfm.202205158.

[8] Thakur, A. K., Mahbub, H., Nowrin, F. H., & Malmali, M. (2022b). Highly Robust Laser-Induced Graphene (LIG) Ultrafiltration Membrane with a Stable Microporous Structure. *ACS Applied Materials & Interfaces*, *14*(41), 46884–46895. https://doi.org/10.1021/acsami.2c09563

[9] Z. Xu *et al.*, "Manipulating Migration Behavior of Magnetic Graphene Oxide via Magnetic Field Induced Casting and Phase Separation toward High-Performance Hybrid Ultrafiltration Membranes," *ACS Appl. Mater. Interfaces*, vol. 8, no. 28, pp. 18418–18429, Jul. 2016, doi: 10.1021/acsami.6b04083.

[10] M. Bayati, H. Peng, H. Deng, J. Lin, and M. Fidalgo de Cortalezzi, "Laser induced graphene /ceramic membrane composite: Preparation and characterization," *J. Membr. Sci.*, vol. 595, p. 117537, Feb. 2020, doi: 10.1016/j.memsci.2019.117537.

[11] Peng, Z., Lin, J., Ye, R., Samuel, E. L. G., & Tour, J. M. (2015b). Flexible and stackable Laser-Induced Graphene supercapacitors. *ACS Applied Materials & Interfaces*, *7*(5), 3414–3419. https://doi.org/10.1021/am509065d

[12] Zhang, J., Zhang, C., Sha, J., Fei, H., Li, Y., & Tour, J. M. (2017c). Efficient Water-Splitting electrodes based on Laser-Induced graphene. *ACS Applied Materials & Interfaces*, *9*(32), 26840–26847. https://doi.org/10.1021/acsami.7b06727

[13] D. V. Lopes, N. F. Santos, J. P. Moura, A. J. S. Fernandes, F. M. Costa, and A. V. Kovalevsky, "Design of laser-induced graphene electrodes for water splitting," *Int. J. Hydrog. Energy*, vol. 48, no. 11, pp. 4158–4172, Feb. 2023, doi: 10.1016/j.ijhydene.2022.11.005.

[14] Md. A. Asgar *et al.*, "Fabrication of Laser-Induced Graphene on Carbon Electrodes for Efficient Hydrogen Evolution Reaction," *Int. J. Energy Res.*, vol. 2024, no. 1, p. 5541306, 2024, doi: 10.1155/2024/5541306.

[15] A. H. Castro Neto, F. Guinea, N. M. R. Peres, K. S. Novoselov, and A. K. Geim, “The electronic properties of graphene,” *Rev. Mod. Phys.*, vol. 81, no. 1, pp. 109–162, Jan. 2009, doi:10.1103/RevModPhys.81.109.

[16] V. Singh, D. Joung, L. Zhai, S. Das, S. I. Khondaker, and S. Seal, “Graphene based materials: Past, present and future,” *Prog. Mater. Sci.*, vol. 56, no. 8, pp. 1178–1271, Oct. 2011, doi: 10.1016/j.pmatsci.2011.03.003.

[17] J. C. Slonczewski and P. R. Weiss, “Band Structure of Graphite,” *Phys. Rev.*, vol. 109, no. 2, pp. 272–279, Jan. 1958, doi: 10.1103/PhysRev.109.272.

[18] P. R. Wallace, “The Band Theory of Graphite,” *Phys. Rev.*, vol. 71, no. 9, pp. 622–634, May 1947, doi: 10.1103/PhysRev.71.622.

[19] Li, X., Tao, L., Chen, Z., Fang, H., Li, X., Wang, X., Xu, J., & Zhu, H. (2017c). Graphene and related two-dimensional materials: Structure-property relationships for electronics and optoelectronics. *Applied Physics Reviews*, *4*(2). https://doi.org/10.1063/1.4983646

[20] “(PDF) Graphene: A review of optical properties and photonic applications.” Accessed: Sep. 07, 2024. [Online]. Available: https://www.researchgate.net/publication/312070999_Graphene_A_review_of_optical_properties_and_photonic_applications

[21] Gan, X., Mak, K. F., Gao, Y., You, Y., Hatami, F., Hone, J., Heinz, T. F., & Englund, D. (2012a). Strong enhancement of Light–Matter interaction in graphene coupled to a photonic crystal nanocavity. *Nano Letters*, *12*(11), 5626–5631. https://doi.org/10.1021/nl302746n

[22] Reina, A., Jia, X., Ho, J., Nezich, D., Son, H., Bulovic, V., Dresselhaus, M. S., & Kong, J. (2008). Large area, Few-Layer graphene films on arbitrary substrates by chemical vapor deposition. *Nano Letters*, *9*(1), 30–35. https://doi.org/10.1021/nl801827v

[23] S. Park and R. S. Ruoff, “Chemical methods for the production of graphenes,” *Nat. Nanotechnol.*, vol. 4, no. 4, pp. 217–224, Apr. 2009, doi: 10.1038/nnano.2009.58.

[24] J. N. Coleman, “Liquid-Phase Exfoliation of Nanotubes and Graphene,” *Adv. Funct. Mater.*, vol. 19, no. 23, pp. 3680–3695, 2009, doi: 10.1002/adfm.200901640.

[25] L. Tang, J. Zhou, D. Zhang, and B. Sheng, “Laser-Induced Graphene Electrodes on Poly(ether–ether–ketone)/PDMS Composite Films for Flexible Strain and Humidity Sensors,” *ACS Appl. Nano Mater.*, vol. 6, no. 19, pp. 17802–17813, Oct. 2023, doi: 10.1021/acsanm.3c03026.

[26] N. Dixit and S. P. Singh, “Laser-Induced Graphene (LIG) as a Smart and Sustainable Material to Restrain Pandemics and Endemics: A Perspective,” *ACS Omega*, vol. 7, no. 6, pp. 5112–5130, Feb. 2022, doi: 10.1021/acsomega.1c06093.

[27] Li, L., Zhang, J., Peng, Z., Li, Y., Gao, C., Ji, Y., Ye, R., Kim, N. D., Zhong, Q., Yang, Y., Fei, H., Ruan, G., & Tour, J. M. (2015c). High-Performance Pseudocapacitive Microsupercapacitors from Laser-Induced Graphene. *Advanced Materials*, *28*(5), 838–845. https://doi.org/10.1002/adma.201503333

[28] Ye, R., James, D. K., & Tour, J. M. (2018f). Laser-Induced graphene. *Accounts of Chemical Research*, *51*(7), 1609–1620. https://doi.org/10.1021/acs.accounts.8b00084

[29] Huang, L., Cheng, L., Ma, T., Zhang, J., Wu, H., Su, J., Song, Y., Zhu, H., Liu, Q., Zhu, M., Zeng, Z., He, Q., Tse, M., Yang, D., Yakobson, B. I., Tang, B. Z., Ren, Y., & Ye, R. (2023c). Direct Synthesis of Ammonia from Nitrate on Amorphous Graphene with Near 100% Efficiency. *Advanced Materials*, *35*(24). https://doi.org/10.1002/adma.202211856

[30] Claro, P. I. C., Pinheiro, T., Silvestre, S. L., Marques, A. C., Coelho, J., Marconcini, J. M., Fortunato, E., Mattoso, L. H. C., & Martins, R. (2022b). Sustainable carbon sources for green laser-induced graphene: A perspective on fundamental principles, applications, and challenges. *Applied Physics Reviews*, *9*(4). https://doi.org/10.1063/5.0100785

[31] Chyan, Y., Ye, R., Li, Y., Singh, S. P., Arnusch, C. J., & Tour, J. M. (2018b). Laser-Induced Graphene by multiple lasing: toward electronics on cloth, paper, and food. *ACS Nano*, *12*(3), 2176–2183. https://doi.org/10.1021/acsnano.7b08539

[32] "Effect of Lignin Content and Extractives on the Higher Heating Value of Wood | Wood and Fiber Science." Accessed: Sep. 07, 2024. [Online]. Available: https://wfs.swst.org/index.php/wfs/article/view/721

[33] Liang, S., & McDonald, A. G. (2014a). Chemical and thermal characterization of potato peel waste and its fermentation residue as potential resources for biofuel and bioproducts production. *Journal of Agricultural and Food Chemistry*, *62*(33), 8421–8429. https://doi.org/10.1021/jf5019406

[34] W. M. A. W. Daud and W. S. W. Ali, "Comparison on pore development of activated carbon produced from palm shell and coconut shell," *Bioresour. Technol.*, vol. 93, no. 1, pp. 63–69, May 2004, doi: 10.1016/j.biortech.2003.09.015.

[35] G. S. Mota *et al.*, "Cellular structure and chemical composition of cork from *Plathymenia reticulata* occurring in the Brazilian Cerrado," *Ind. Crops Prod.*, vol. 90, pp. 65–75, Nov. 2016, doi: 10.1016/j.indcrop.2016.06.014.

[36] Wang, L., Wang, Z., Bakhtiyari, A. N., & Zheng, H. (2020e). A Comparative Study of Laser-Induced Graphene by CO2 Infrared Laser and 355 nm Ultraviolet (UV) Laser. *Micromachines*, *11*(12), 1094. https://doi.org/10.3390/mi11121094

[37] "Polyimide (PI) - Uses, Structure, Properties & Applications." Accessed: Sep. 07, 2024. [Online]. Available: https://omnexus.specialchem.com/selection-guide/polyimide-pi-plastic

[38] I. Sava *et al.*, "Electrical and mechanical properties of polyimide films treated by plasma formed in water and isopropanol," *React. Funct. Polym.*, vol. 134, pp. 22–30, Jan. 2019, doi: 10.1016/j.reactfunctpolym.2018.11.005.

[39] Sullivan, K. (n.d.-c). *Kapton® Polyimide Film's extraordinary properties*. https://blog.marianinc.com/blog/kapton-polyimide-film

[40] *DuPont^{TM} Kapton® polyimide films*. (n.d.-c). https://www.dupont.com/electronics-industrial/kapton-polyimide-film.html

[41] Wang, C., Zhao, X., Tian, D., Wang, D., Chen, C., & Zhou, H. (2016c). Synthesis and characterization of novel polyimides derived from 4,4'-bis(5-amino-2-pyridinoxy)benzophenone: effect of pyridine and ketone units in the main. *Designed Monomers & Polymers*, *20*(1), 97–105. https://doi.org/10.1080/15685551.2016.1231036

[42] S. Movaghgharnezhad and P. Kang, "Laser-induced graphene: synthesis advances, structural tailoring, enhanced properties, and sensing applications," *J. Mater. Chem. C*, vol. 12, no. 19, pp. 6718–6742, May 2024, doi: 10.1039/D3TC04677J.

[43] W. Ma, J. Zhu, Z. Wang, W. Song, and G. Cao, "Recent advances in preparation and application of laser-induced graphene in energy storage devices," *Mater. Today Energy*, vol. 18, p. 100569, Dec. 2020, doi: 10.1016/j.mtener.2020.100569.

[44] Vivaldi, F. M., Dallinger, A., Bonini, A., Poma, N., Sembranti, L., Biagini, D., Salvo, P., Greco, F., & Di Francesco, F. (2021b). Three-Dimensional (3D) Laser-Induced graphene: structure, properties, and application to chemical sensing. *ACS Applied Materials & Interfaces*, *13*(26), 30245–30260. https://doi.org/10.1021/acsami.1c05614

[45] K. Settu, P.-T. Chiu, and Y.-M. Huang, "Laser-Induced Graphene-Based Enzymatic Biosensor for Glucose Detection," *Polymers*, vol. 13, no. 16, Art. no. 16, Jan. 2021, doi: 10.3390/polym13162795.

[46] Guo, Y., Zhang, C., Chen, Y., & Nie, Z. (2022g). Research progress on the preparation and applications of Laser-Induced Graphene Technology. *Nanomaterials*, *12*(14), 2336. https://doi.org/10.3390/nano12142336

[47] Q. Shu *et al.*, "Flexible resistive tactile pressure sensors," *J. Mater. Chem. A*, vol. 12, no. 16, pp. 9296–9321, Apr. 2024, doi: 10.1039/D3TA06976A.

[48] A. Nag, S. C. Mukhopadhyay, and J. Kosel, "Wearable Flexible Sensors: A Review," *IEEE Sens. J.*, vol. 17, no. 13, pp. 3949–3960, Jul. 2017, doi: 10.1109/JSEN.2017.2705700.

[49] Xu, J., Pan, J., Cui, T., Zhang, S., Yang, Y., & Ren, T. (2023c). Recent progress of tactile and force sensors for Human–Machine interaction. *Sensors*, *23*(4), 1868. https://doi.org/10.3390/s23041868

[50] Huang, F., Yan, Z., Zhou, S., Gu, B., Wang, S., Wang, S., & Zhou, S. (2023a). Copper electrode preparation by a selective laser reduction of copper oxide on lignin fiber membranes and its application as a photodetector. *Optics Express*, *31*(5), 8190. https://doi.org/10.1364/oe.486114

[51] Qu, M., Tian, Y., Cheng, Y., Zhong, J., & Zhang, C. (2022c). Whole-Device Mass-Producible perovskite photodetector based on Laser-Induced graphene electrodes. *Advanced Optical Materials*, *10*(24). https://doi.org/10.1002/adom.202201741

[52] J. Alda, "Laser and Gaussian Beam Propagation and Transformation," *Encycl. Opt. Eng.*, Jan. 2003.

[53] D. R. Paschotta, "The RP Photonics Encyclopedia." Accessed: Sep. 07, 2024. [Online]. Available: https://www.rp-photonics.com/encyclopedia.html

[54] H. Kogelnik, "CHAPTER 6 - Propagation of Laser Beams," in *Applied Optics and Optical Engineering*, vol. 7, R. R. Shannon and J. C. Wyant, Eds., Elsevier, 1979, pp. 155–190. doi: 10.1016/B978-0-12-408607-4.50013-X.

[55] Kogelnik, H. (1965b). On the Propagation of Gaussian Beams of Light Through Lenslike Media Including those with a Loss or Gain Variation. *Applied Optics*, *4*(12), 1562. https://doi.org/10.1364/ao.4.001562

[56] Kogelnik, H., & Li, T. (1966b). Laser beams and resonators. *Applied Optics*, *5*(10), 1550. https://doi.org/10.1364/ao.5.001550

[57] Schneiter, F., Rätzel, D., & Braun, D. (2018a). The gravitational field of a laser beam beyond the short wavelength approximation. *Classical and Quantum Gravity*, *35*(19), 195007. https://doi.org/10.1088/1361-6382/aadc81

[58] B. Shiner, "Fiber lasers for material processing," in *Critical Review: Industrial Lasers and Applications*, SPIE, Mar. 2005, pp. 60–68. doi: 10.1117/12.601648.

[59] I. P. G. Photonics, "Fiber Laser Sources & Solutions | IPG Photonics," IPG Photonics Corporation. Accessed: Sep. 07, 2024. [Online]. Available: https://www.ipgphotonics.com/

[60] Deng, B., Wang, Z., Liu, W., & Hu, B. (2023c). Multifunctional motion sensing enabled by Laser-Induced graphene. *Materials*, *16*(19), 6363. https://doi.org/10.3390/ma16196363

[61] Fiodorov, V., Trusovas, R., Mockus, Z., Ratautas, K., & Račiukaitis, G. (2023f). Laser-Induced graphene formation on polyimide using UV to Mid-Infrared laser radiation. *Polymers*, *15*(21), 4229. https://doi.org/10.3390/polym15214229

[62] Murray, R., Burke, M., Iacopino, D., & Quinn, A. J. (2021d). Design of experiments and optimization of Laser-Induced graphene. *ACS Omega*, *6*(26), 16736–16743. https://doi.org/10.1021/acsomega.1c00309

[63] D. Kwak *et al.*, "Investigation of Laser-Induced Graphene (LIG) on a Flexible Substrate and Its Functionalization by Metal Doping for Gas-Sensing Applications," *Int. J. Mol. Sci.*, vol. 25, no. 2, Art. no. 2, Jan. 2024, doi: 10.3390/ijms25021172.

[64] Ferrari, A. C., & Robertson, J. (2000b). Interpretation of Raman spectra of disordered and amorphous carbon. *Physical Review. B, Condensed Matter*, *61*(20), 14095–14107. https://doi.org/10.1103/physrevb.61.14095

[65] R. Arul, R. N. Oosterbeek, J. Robertson, G. Xu, J. Jin, and M. C. Simpson, "The mechanism of direct laser writing of graphene features into graphene oxide films involves photoreduction and thermally assisted structural rearrangement," *Carbon*, vol. 99, pp. 423–431, Apr. 2016, doi: 10.1016/j.carbon.2015.12.038.

[66] S. Y. Kim, J. H. Kim, K. N. Kim, H. Oh, S. Myung, and D. H. Kim, "Highly conductive, conformable ionic laser-induced graphene electrodes for flexible iontronic devices," *Sci. Rep.*, vol. 14, no. 1, p. 4599, Feb. 2024, doi: 10.1038/s41598-024-55082-w.

[67] Zhang, W., Lai, W., & Cao, R. (2016b). Energy-Related small molecule activation reactions: oxygen reduction and hydrogen and oxygen evolution reactions catalyzed by Porphyrin- and Corrole-Based systems. *Chemical Reviews*, *117*(4), 3717–3797. https://doi.org/10.1021/acs.chemrev.6b00299

[68]Idriss, H. (2020a). Hydrogen production from water: past and present. *Current Opinion in Chemical Engineering*, *29*, 74–82. https://doi.org/10.1016/j.coche.2020.05.009

[69] A. Charisiadis *et al.*, "Photoelectrochemical properties of dyads composed of porphyrin/ruthenium catalyst grafted on metal oxide semiconductors," *Dyes Pigments*, vol. 185, p. 108908, Feb. 2021, doi: 10.1016/j.dyepig.2020.108908.

[70] H. M. Castro-Cruz and N. A. Macías-Ruvalcaba, "Porphyrin-catalyzed electrochemical hydrogen evolution reaction. Metal-centered and ligand-centered mechanisms," *Coord. Chem. Rev.*, vol. 458, p. 214430, May 2022, doi: 10.1016/j.ccr.2022.214430.

[71] Choi, W. I., Wood, B. C., Schwegler, E., & Ogitsu, T. (2015b). Combinatorial search for High-Activity hydrogen catalysts based on Transition-Metal-Embedded graphitic carbons. *Advanced Energy Materials*, *5*(23). https://doi.org/10.1002/aenm.201501423

[72] A. Baby, L. Trovato, and C. Di Valentin, "Single Atom Catalysts (SAC) trapped in defective and nitrogen-doped graphene supported on metal substrates," *Carbon*, vol. 174, pp. 772–788, Apr. 2021, doi: 10.1016/j.carbon.2020.12.045.

[73] B. Beyene and chen-H. Hung, "Recent progress on metalloporphyrin-based hydrogen evolution catalysis," *Coord. Chem. Rev.*, vol. 410, p. 213234, May 2020, doi: 10.1016/j.ccr.2020.213234.

[74] Admin, "Peak Power and Average Power in ns and Sub-ns Lasers," Solid State Lasers and Laser Diodes from RPMC Lasers Inc. Accessed: Sep. 10, 2024. [Online]. Available: https://www.rpmclasers.com/blog/peak-power-and-average-power-in-ns-and-sub-ns-lasers/

[75] Mayorga-Cruz, D., & Melnikov, I. V. (2001). Kinetics of a solid-state laser with polarizable saturable absorber. *Optics Express*, *9*(9), 428. https://doi.org/10.1364/oe.9.000428

[76] Verma, S., Kehrer, T., Hesser, J., & Mosquera, S. A. (2019). Analysis of Impact of Humidity and Temperature on Excimer Laser Ablation of Polyethylene Terephthalate, Polymethylmethacrylate, and Porcine Corneal Tissue. *Lasers in Surgery and Medicine*, *52*(7), 627–638. https://doi.org/10.1002/lsm.23190

[77] D. Kwon, E. Park, S. Ha, and N. Kim, "Effect of humidity changes on dimensional stability of 3D printed parts by selective laser sintering," *Int. J. Precis. Eng. Manuf.*, vol. 18, no. 9, pp. 1275–1280, Sep. 2017, doi: 10.1007/s12541-017-0150-0.

[78] K. Murari, "Unveiling the Key Parameters that Define Laser Diode Performance," Prophotonix. Accessed: Sep. 10, 2024. [Online]. Available: https://www.prophotonix.com/blog/unveiling-the-key-parameters-that-define-laser-diode-performance/

[79] R. Trusovas, K. Ratautas, G. Račiukaitis, and G. Niaura, "Graphene layer formation in pinewood by nanosecond and picosecond laser irradiation," *Appl. Surf. Sci.*, vol. 471, pp. 154–161, Mar. 2019, doi: 10.1016/j.apsusc.2018.12.005.

[80] G. G. Gladush and I. Smurov, "Plasma Phenomena in Laser Processing of Materials," in *Physics of Laser Materials Processing: Theory and Experiment*, G. G. Gladush and I. Smurov, Eds., Berlin, Heidelberg: Springer, 2011, pp. 145–210. doi: 10.1007/978-3-642-19831-1_3.

[81] A. Sartanavičius, J. Žemgulytė, P. Ragulis, K. Ratautas, and R. Trusovas, "Laser-Induced Graphene in Polyimide for Antenna Applications," *Crystals*, vol. 13, no. 7, Art. no. 7, Jul. 2023, doi: 10.3390/cryst13071003.

[82] M. Liu, J. Wu, and H. Cheng, "Effects of laser processing parameters on properties of laser-induced graphene by irradiating CO2 laser on polyimide," *Sci. China Technol. Sci.*, vol. 65, no. 1, pp. 41–52, Jan. 2022, doi: 10.1007/s11431-021-1918-8.

[83] *Probe Station: I-V Curves with Keithley 2400 and Python Script - UCSB Nanofab Wiki*. (n.d.). https://wiki.nanofab.ucsb.edu/wiki/Probe_Station:_I-V_Curves_with_Keithley_2400_and_Python_Script

[84]*IV Characterization of photovoltaic cells & panels*. (n.d.-c). Tektronix. https://www.tek.com/en/documents/application-note/i-v-characterization-photovoltaic-cells-and-panels-using-keithley-2450-or

[85] L. Cheng *et al.*, "Flash healing of laser-induced graphene," *Nat. Commun.*, vol. 15, no. 1, p. 2925, Apr. 2024, doi: 10.1038/s41467-024-47341-1.

[86] DuPont. (n.d.). *DuPont^{TM} Kapton® Summary of Properties*.

[87] Santos, E. M., Sheng, W., Salmani, R. E., Nick, S. T., Ghanbarpour, A., Gholami, H., Vasileiou, C., Geiger, J. H., & Borhan, B. (2021d). Design of large stokes shift fluorescent proteins based on excited state proton transfer of an engineered photobase. *Journal of the American Chemical Society*, *143*(37), 15091–15102. https://doi.org/10.1021/jacs.1c05039

[88]Bhattacharya, G., Fishlock, S. J., Hussain, S., Choudhury, S., Xiang, A., Kandola, B., Pritam, A., Soin, N., Roy, S. S., & McLaughlin, J. A. (2022c). Disposable Paper-Based Biosensors: Optimizing the electrochemical properties of Laser-Induced graphene. *ACS Applied Materials & Interfaces*, *14*(27), 31109–31120. https://doi.org/10.1021/acsami.2c06350

[89]Romano, V., Torrisi, L., Cutroneo, M., Havranek, V., & D'Angelo, G. (2018c). Raman investigation of laser-induced structural defects of graphite oxide films. *EPJ Web of Conferences*, *167*, 04011. https://doi.org/10.1051/epjconf/201816704011

[90] L. Wang, K. Yin, Q. Deng, Q. Huang, and C. J. Arnusch, “Multiscale hybrid-structured femtosecond laser-induced graphene with outstanding photo-electro-thermal effects for all-day anti-icing/deicing,” *Carbon*, vol. 219, p. 118824, Feb. 2024, doi: 10.1016/j.carbon.2024.118824.

[91] Y. Lee *et al.*, “Ultra-thin light-weight laser-induced-graphene (LIG) diffractive optics,” *Light Sci. Appl.*, vol. 12, no. 1, p. 146, Jun. 2023, doi: 10.1038/s41377-023-01143-0.

[92] Wang, L., Wang, Z., Bakhtiyari, A. N., & Zheng, H. (2020f). A Comparative Study of Laser-Induced Graphene by CO2 Infrared Laser and 355 nm Ultraviolet (UV) Laser. *Micromachines*, *11*(12), 1094. https://doi.org/10.3390/mi11121094

[93]Duley, W. W. (1996b). Photochemical and photothermal effects. In *Cambridge University Press eBooks* (pp. 78–97). https://doi.org/10.1017/cbo9780511524134.004

[94] Y.-S. Hsiao *et al.*, “Lightweight Flexible Polyimide-Derived Laser-Induced Graphenes for High-Performance Thermal Management Applications,” *Chem. Eng. J.*, vol. 451, p. 138656, Jan. 2023, doi: 10.1016/j.cej.2022.138656.

[95] Banhart, F. (2019d). Elemental carbon in the sp1 hybridization. *ChemTexts*, *6*(1). https://doi.org/10.1007/s40828-019-0098-z

[96] Libretexts. (2023c, May 3). *1.2: Chemical bonding*. Chemistry LibreTexts. https://chem.libretexts.org/Bookshelves/Inorganic_Chemistry/Introduction_to_Solid_State_Chemistry/01%3A_Lectures/1.02%3A_Chemical_Bonding

[97] Liu, J., Bao, S., & Wang, X. (2022b). Applications of Graphene-Based Materials in Sensors: a review. *Micromachines*, *13*(2), 184. https://doi.org/10.3390/mi13020184

[98] Jeong, S., Ma, Y., Lee, J., Je, G., & Shin, B. (2019b). Flexible and Highly Sensitive Strain Sensor Based on Laser-Induced Graphene Pattern Fabricated by 355 nm Pulsed Laser. *Sensors*, *19*(22), 4867. https://doi.org/10.3390/s19224867

[99] G. Li, “Direct laser writing of graphene electrodes,” *J. Appl. Phys.*, vol. 127, no. 1, p. 010901, Jan. 2020, doi: 10.1063/1.5120056.

[100] Inagaki, M., Harada, S., Sato, T., Nakajima, T., Horino, Y., & Morita, K. (1989b). Carbonization of polyimide film “Kapton.” *Carbon*, *27*(2), 253–257. https://doi.org/10.1016/0008-6223(89)90131-0

[101] Stanford, M. G., Zhang, C., Fowlkes, J. D., Hoffman, A., Ivanov, I. N., Rack, P. D., & Tour, J. M. (2020b). High-Resolution Laser-Induced Graphene. Flexible Electronics beyond the Visible Limit. *ACS Applied Materials & Interfaces*, *12*(9), 10902–10907. https://doi.org/10.1021/acsami.0c01377

[102] H. Yoon *et al.*, “A chemically modified laser-induced porous graphene based flexible and ultrasensitive electrochemical biosensor for sweat glucose detection,” *Sens. Actuators B Chem.*, vol. 311, p. 127866, May 2020, doi: 10.1016/j.snb.2020.127866.

[103] W. Yan, W. Yan, T. Chen, J. Xu, Q. Tian, and D. Ho, “Size-Tunable Flowerlike MoS2 Nanospheres Combined with Laser-Induced Graphene Electrodes for NO2 Sensing,” *ACS Appl. Nano Mater.*, vol. 3, no. 3, pp. 2545–2553, Mar. 2020, doi: 10.1021/acsanm.9b02614.

[104] Rahimi, R., Ochoa, M., Yu, W., & Ziaie, B. (2015a). Highly stretchable and sensitive unidirectional strain sensor via laser carbonization. *ACS Applied Materials & Interfaces*, *7*(8), 4463–4470. https://doi.org/10.1021/am509087u

[105] X. Xuan, J. Y. Kim, X. Hui, P. S. Das, H. S. Yoon, and J.-Y. Park, “A highly stretchable and conductive 3D porous graphene metal nanocomposite based electrochemical-physiological hybrid biosensor,” *Biosens. Bioelectron.*, vol. 120, pp. 160–167, Nov. 2018, doi: 10.1016/j.bios.2018.07.071.

[106] Bressi, A. C., Dallinger, A., Steksova, Y., & Greco, F. (2023b). Bioderived Laser-Induced graphene for sensors and supercapacitors. *ACS Applied Materials & Interfaces*, *15*(30), 35788–35814. https://doi.org/10.1021/acsami.3c07687

[107] Z. Li *et al.*, “Preparation of Laser-Induced Graphene Fabric from Silk and Its Application Examples for Flexible Sensor,” *Adv. Eng. Mater.*, vol. 23, no. 9, p. 2100195, 2021, doi: 10.1002/adem.202100195.

[108] R. Ye *et al.*, “Laser-Induced Graphene Formation on Wood,” *Adv. Mater.*, vol. 29, no. 37, p. 1702211, 2017, doi: 10.1002/adma.201702211.

[109] C. Lew, “Nitrogen-doped Graphene by Plasma Treatment,” Harrick Plasma. Accessed: Sep. 08, 2024. [Online]. Available: https://harrickplasma.com/nitrogen-doped-graphene-by-plasma-treatment/

[110] Santhosh, N. M., Filipič, G., Kovacevic, E., Jagodar, A., Berndt, J., Strunskus, T., Kondo, H., Hori, M., Tatarova, E., & Cvelbar, U. (2020c). N-Graphene nanowalls via plasma nitrogen incorporation and substitution: the experimental evidence. *Nano-Micro Letters*, *12*(1). https://doi.org/10.1007/s40820-020-0395-5

[111] X.-F. Li *et al.*, “Unraveling the formation mechanism of graphitic nitrogen-doping in thermally treated graphene with ammonia,” *Sci. Rep.*, vol. 6, no. 1, p. 23495, Mar. 2016, doi: 10.1038/srep23495.

[112] Bigras, G. R., Glad, X., Vinchon, P., Martel, R., & Stafford, L. (2020c). Selective nitrogen doping of graphene due to preferential healing of plasma-generated defects near grain boundaries. *Npj 2D Materials and Applications*, *4*(1). https://doi.org/10.1038/s41699-020-00176-y

[113] Vesel, A., Zaplotnik, R., Primc, G., & Mozetič, M. (2020c). A review of strategies for the synthesis of N-Doped Graphene-Like Materials. *Nanomaterials*, *10*(11), 2286. https://doi.org/10.3390/nano10112286

[114] Begley, A., Bartolomeo, G. L., Abbott, D. F., Mougel, V., & Zenobi, R. (2023c). Nitrogen-doping graphene at ambient conditions with N2-DBD-plasma and the role of neutral species. *Plasma Processes and Polymers*, *21*(4). https://doi.org/10.1002/ppap.202300168

[115] S. Raha and M. Ahmaruzzaman, “ZnO nanostructured materials and their potential applications: progress, challenges and perspectives,” *Nanoscale Adv.*, vol. 4, no. 8, pp. 1868–1925, Apr. 2022, doi: 10.1039/D1NA00880C.

[116] Del Rocío López Guemez, A., García, A. C., López, J. L. C., Vidal, H. P., & Flores, L. L. D. (2023). Evaluation of the photocatalytic activity of ZnO nanorods and nanoflowers grown from seed layers deposited by spin coating. *Boletín De La Sociedad Española De Cerámica Y Vidrio*. https://doi.org/10.1016/j.bsecv.2023.06.003

[117] S. Fiedler, C. Ton-That, and M. R. Phillips, “Defect-free ZnO nanorods with high angular distribution for enhanced excitonic emission,” *J. Mater. Res.*, vol. 38, no. 8, pp. 2145–2155, Apr. 2023, doi: 10.1557/s43578-023-00941-x.

[118] Aspoukeh, P. K., Barzinjy, A. A., & Hamad, S. M. (2021c). Synthesis, properties and uses of ZnO nanorods: a mini review. *International Nano Letters.*, *12*(2), 153–168. https://doi.org/10.1007/s40089-021-00349-7

[119] Y. Yang, Q. Huang, G. F. Payne, R. Sun, and X. Wang, “A highly conductive, pliable and foldable Cu/cellulose paper electrode enabled by controlled deposition of copper nanoparticles,” *Nanoscale*, vol. 11, no. 2, pp. 725–732, Jan. 2019, doi: 10.1039/C8NR07123C.

[120] Yi, J., Chen, J., Yang, Z., Dai, Y., Li, W., Cui, J., Ciucci, F., Lu, Z., & Yang, C. (2019c). Facile Patterning of Laser-Induced Graphene with Tailored Li Nucleation Kinetics for Stable Lithium-Metal Batteries. *Advanced Energy Materials*, *9*(38). https://doi.org/10.1002/aenm.201901796

[121] Yang, Z., Xu, C., Yan, H., Liu, Y., Yue, C., Zhang, L., Shui, M., Hu, F., & Shu, J. (2021b). Laser-Induced graphene assisting Self-Conversion reaction for Sulfur-Free aqueous CU-S battery. *Advanced Functional Materials*, *31*(46). https://doi.org/10.1002/adfm.202103893

[122] Hernandez, J. L., & Woodrow, K. A. (2022a). Medical applications of porous biomaterials: features of porosity and Tissue-Specific implications for biocompatibility. *Advanced Healthcare Materials*, *11*(9). https://doi.org/10.1002/adhm.202102087